

# Quantum-metric-induced giant and reversible nonreciprocal transport phenomena in chiral loop-current phases of kagome metals

Rina Tazai<sup>1</sup>, Youichi Yamakawa<sup>2</sup>, Takahiro Morimoto<sup>3</sup> and Hiroshi Kontani<sup>2</sup>

<sup>1</sup>*Yukawa Institute for Theoretical Physics, Kyoto University, Kyoto 606-8502, Japan*

<sup>2</sup>*Department of Physics, Nagoya University, Nagoya 464-8602, Japan*

<sup>3</sup>*Department of Applied Physics, The University of Tokyo, Tokyo 113-8656, Japan*

(Dated: August 9, 2024)

Rich spontaneous symmetry-breaking phenomena with nontrivial quantum geometric properties in metals represent central issues in condensed matter physics. The emergence of chiral loop-current order, accompanied by time-reversal symmetry (TRS) breaking in various kagome metals, has garnered significant attention as a novel quantum topological state. Particularly noteworthy is the giant electrical magnetochiral anisotropy (eMChA) in CsV<sub>3</sub>Sb<sub>5</sub> [Guo et al, Nature 611, 461 (2022)], which provides compelling evidence of TRS and inversion-symmetry breaking. However, the underlying essence of this observation has remained obscured due to the lack of theoretical understanding. Here, we identify that the chiral loop-current induces substantial and switchable eMChA in kagome metals by taking account of the experimentally observed stripe charge-density-wave. The obtained eMChA coefficient is  $\gamma_{\text{eM}} \propto M_{\text{orb}}\tau$ , where  $M_{\text{orb}}$  is the loop-current-induced orbital magnetization and  $\tau$  is the lifetime of conduction electrons. Importantly, giant eMChA arises from the quantum metric (QM), which defines essential quantum phases of matter and their unique functionalities, including nonlinear effects. This effect is resonantly amplified in the loop-current phase, and the derived eMChA is switched by minute magnetic fields. This research elucidates the fundamental symmetry breaking in kagome metals and also sets the stage for investigating the QM-induced phenomena arising from electronic correlations.

## INTRODUCTION

In the realm of condensed matter physics, the investigation of quantum phase transitions and spontaneous symmetry breaking provides fundamental insights into the essential behaviors of electrons within solids. The exploration of rotational symmetry, time-reversal symmetry (TRS), inversion symmetry (IS), and U(1) gauge symmetry-breaking quantum states has been actively pursued in various strongly correlated metals [1–5]. The discovery of kagome-lattice metals AV<sub>3</sub>Sb<sub>5</sub> ( $A=\text{K, Rb, Cs}$ ) has paved the way for investigating novel correlation-driven quantum states and superconductivity [6–12]. Unconventional multiple-phase transitions, both with and without TRS, arise due to the suppression of conventional spin or charge density waves (DWs) by geometrical frustration. The emergence of the 2×2 Star-of-David or Tri-Hexagonal DW is attributed to the triple- $\mathbf{q}$  (3Q) bond order (BO), wherein three BOs coexist at wavevectors  $\mathbf{q} = \mathbf{q}_1, \mathbf{q}_2, \mathbf{q}_3$ . This BO phase hosts intriguing chiral charge loop-current (LC) orders that violate TRS [9, 10], alongside unconventional superconductivity [6–8, 11, 12]. Various theoretical studies have been undertaken to comprehend such TRS breaking multiple-orders [13–18]. The BO quantum fluctuation mechanism for the LC and superconductivity has been developed in Refs. [19, 20].

Recently, serious efforts have been devoted to the measurements of the LC order. The staggered local magnetic field due to the LC order has been observed by several  $\mu\text{SR}$  studies [21–24]. Importantly, the 3Q LC state has chirality, which gives rise to tiny residual uniform orbital magnetization  $M_{\text{orb}}$ . Therefore, the 3Q LC order is mag-

nified under  $B_z$  [25, 26], and its chirality is switched by tiny  $B_z$  as observed by the anomalous Hall effect (AHE) [27, 28], nonreciprocal transport [29], STM [9, 10], and Kerr rotation [30] measurements. Interestingly, recent magnetic torque measurements [31] reveal the emergence of the 1Q-LC order above  $T_{\text{BO}}$ , and the 1Q  $\rightarrow$  3Q LC transition occurs under the conical magnetic field. Because  $M_{\text{orb}} = 0$  in the 1Q-LC state due to its global TRS, this scenario does not conflict with previous studies [9, 21–24, 29, 30]. Notably, the LC will also have significant impact on the superconductivity, such as leading the pair-density-wave (PDW) and the 4e, 6e pairing states [32–34].

Nonlinear effects in bulk materials provide a probe of the symmetry and geometry of Bloch electrons in solids and also useful functionalities including rectification and frequency conversion, which makes nonlinear effects important in both fundamental physics and application purposes [35–37]. Nonreciprocal transport is a current rectification effect in IS broken systems. In particular, nonreciprocal current under the applied magnetic field is called electrical magnetochiral anisotropy (eMChA) and is intensively studied [38–41]. Recently, giant eMChA coefficient  $\gamma_{\text{eM}}$  in  $\rho_{zz} = \rho_{zz}^0(1 + \gamma_{\text{eM}}B_xJ_z)$  has been discovered in CsV<sub>3</sub>Sb<sub>5</sub> in Ref. [29]. The observation clearly indicates the IS breaking, by considering the inversion operation that induces  $\mathbf{j} \rightarrow -\mathbf{j}$  and  $\mathbf{B} \rightarrow \mathbf{B}$ . The observed  $\gamma_{\text{eM}}$  in CsV<sub>3</sub>Sb<sub>5</sub> is one or two orders of magnitude larger than the chiral magnets, such as CrNb<sub>3</sub>S<sub>6</sub> [42] and MnSi [43], in which the chiral spin texture gives the eMChA. Unfortunately, the fundamental electronic states of the LC phase indicated by this important experiment are

still unclear because of the lack of the underlying microscopic mechanism of the eMChA.

The observed giant eMChA and AHE manifest that kagome metal is an ideal platform for developing quantum geometric effects, considering that quantum geometry defines essential quantum phases of matter and their unique functionalities, including nonlinear effects [47–52]. Nontrivial geometry of the Bloch electrons in solids is captured by the quantum geometric tensor  $\mathcal{T} = G - i\Omega/2$  that measures the distance of the Bloch wave functions for different momenta in the Hilbert space [48, 49]. The imaginary part  $\Omega$  is the Berry curvature that gives rise to the anomalous (or spin) Hall effects [52–55] and nonlinear Hall effect [56]. The real part  $G$  is the quantum metric (QM) and characterizes, for example, wave functions in flat bands, superfluid weight [57], and nonlinear transport [58]. In kagome metals,  $\Omega$  causes the large anomalous Hall effect [20, 59] and orbital magnetization [25], while the impact of the QM in kagome metals is still uncovered. Importantly, in kagome metals,  $\mathcal{T}$  originates from nontrivial quantum orders such as the BO and LC: Their microscopic mechanisms have been developed for cuprates and Fe-based superconductors [1–5, 60–71], twisted bilayer graphene [72, 73], and kagome metals [13–17, 19, 20, 74, 75].

In this study, we investigate the mechanism underlying the giant and field-tunable eMChA arising from chiral LC in kagome metals, with a particular focus on the  $2a_0$  or  $4a_0$  stripe charge DW (CDW) that is universally observed in Cs-based kagome metals by STM and NMR measurements [44, 45]. Here,  $a_0$  denotes the unit cell length. The realized electronic states, characterized by TRS and IS breaking, lead to a large eMChA coefficient  $\gamma_{\text{eM}} \propto M_{\text{orb}}\tau I_{\text{st}}$ , where  $I_{\text{st}}$  is the stripe CDW potential and  $\tau$  is the lifetime of conduction electrons. The driving force behind the giant eMChA in kagome metals stems from the TRS-odd component of the QM, which experiences resonant enhancement due to significant inter-band reconstruction in the LC phase. Crucially, the derived eMChA exhibits a sharp change in sign upon variation of the small magnetic field  $B_z$ , consistent with observations in Cs-based kagome metals. The discovered QM-induced eMChA mechanism provides crucial insights into the electronic structure and symmetry characteristics of multi-quantum orders of kagome metals.

## RESULTS

### 2D kagome lattice model: LC+BO order parameters

In this paper, we study the eMChA conductivity in 3D kagome lattice models with  $2 \times 2 \times 2$  orders, in which the unit cell contains 24 V sites. The unit cell on each

layer contains 12 V sites; see Figs. 1 **a** and **b**. Here, we consider two important  $d$ -orbitals: The orbital  $d_p$  ( $= d_{xz}$ ) composes the “pure-type” bands and the orbital  $d_m$  ( $= d_{yz}$ ) composes the “mix-type” bands.  $d_p$  and  $d_m$  orbitals are shown in Fig. 1 **b**. Both BO and LC orders are expected to appear on the  $d_p$  orbital [19, 20] because the pure-type band is strongly correlated due to its narrow bandwidth. In the present model, the mix-type FS contains  $\lesssim 15\%$   $d_p$ -orbital component. In the DFT bandstructure of CsV<sub>5</sub>Sb<sub>5</sub>, the mix-type FS contains 10 ~ 30%  $d_p$ -orbital component, and the pure-type FS contains 5 ~ 10%  $d_m$ -orbital component. Such ( $d_p$ ,  $d_m$ ) orbital mixture on the FSs is explained in Ref. [25] in detail. For this reason, prominent reconstruction between pure-FS and mix-FS is caused by the LC order parameter on  $d_p$ -orbitals. This fact leads to the resonantly magnified QM  $G^{zz}$  at the Fermi level as we will explain below.

To begin with, we consider the 2D kagome lattice model with  $2 \times 2$  orders. The unit cell of the 2D kagome lattice is composed of the sublattices A, B, C shown in Fig. 1 **a**. The three wavevectors are given as  $\mathbf{q}_1 = \pi\mathbf{a}_{\text{AB}} \times \hat{z}/S$ ,  $\mathbf{q}_2 = \pi\mathbf{a}_{\text{BC}} \times \hat{z}/S$ , and  $\mathbf{q}_3 = \pi\mathbf{a}_{\text{CA}} \times \hat{z}/S$ , where  $S = \sqrt{3}a_0^2/2$  is the area of the original unit cell. (Here,  $a_0 = 2|\mathbf{a}_{\text{AB}}|$ .) In the  $3Q$  LC state, the unit cell is enlarged to  $2 \times 2$  which is composed of 12 sites, as shown in Fig. 1 **a**. The form factor ( $=$ normalized  $\delta t_{ij}^c$ ) with  $\mathbf{q} = \mathbf{q}_1$ ,  $f_{ij}^{(1)}$ , is  $+i$  when  $(i, j)$  belongs to the sites  $(l, m) = (1, 2), (2, 4), (4, 5), (5, 1)$ , and  $-i$  for  $(7, 8), (8, 10), (10, 11), (11, 7)$ . Importantly, the odd parity relation  $f_{ij}^{(1)} = -f_{ji}^{(1)}$  holds for the LC. Other form factors with  $\mathbf{q}_2$  and  $\mathbf{q}_3$ ,  $f_{ij}^{(2)}$  and  $f_{ij}^{(3)}$ , are also derived from Fig. 1 **a**. Using the notation  $\mathbf{f}_{ij} = (f_{ij}^{(1)}, f_{ij}^{(2)}, f_{ij}^{(3)})$ , the LC form factor is given as

$$\delta t_{ij}^c = \boldsymbol{\eta} \cdot \mathbf{f}_{ij}, \quad (1)$$

where  $\boldsymbol{\eta} \equiv (\eta_1, \eta_2, \eta_3)$  is the set of current order parameters with the wavevector  $\mathbf{q}_m$ . Note that the LC form factors are Hermitian  $\delta t_{ij}^{lm} = (\delta t_{ji}^{ml})^*$ , which leads to the relation  $f_{\mathbf{q}}^{lm}(\mathbf{k}) = (f_{-\mathbf{q}}^{ml}(\mathbf{k} + \mathbf{q}))^*$  [5].

Also, the BO form factor shown in Fig. 1 **b** is given as

$$\delta t_{ij}^b = \boldsymbol{\phi} \cdot \mathbf{g}_{ij}, \quad (2)$$

where  $\boldsymbol{\phi} \equiv (\phi_1, \phi_2, \phi_3)$  is the set of BO parameters with the wavevector  $\mathbf{q}_m$ , and  $g_{ij}^{(m)} = g_{ji}^{(m)} = +1$  or  $-1$  as shown in Fig. 1 **b**. For example,  $g_{ij}^{(1)} = +1$  [ $-1$ ] for  $(i, j)$  belongs to  $(1, 2), (4, 5), (8, 10), (11, 7)$  [ $(2, 4), (5, 1), (7, 8), (10, 11)$ ]. Here, we introduce the notation  $\mathbf{e}_0 = (1, 1, 1)/\sqrt{3}$ ,  $\mathbf{e}_a = (1, -1, -1)/\sqrt{3}$ ,  $\mathbf{e}_b = (-1, 1, -1)/\sqrt{3}$ ,  $\mathbf{e}_c = (-1, -1, 1)/\sqrt{3}$ . The  $3Q$ -LC order and the  $3Q$ -BO are respectively expressed as  $\phi_l \equiv \phi \mathbf{e}_l$  and  $\boldsymbol{\eta}_l \equiv \eta \mathbf{e}_l$ , where  $l = 0, a \sim c$ .

Figure 1 **c** depicts the original “pure-type” Fermi surface (FS) composed of the  $d_p$  orbital in the absence of the

density waves, expressed in the original Brillouin zone (BZ). The reconstructed FSs under the  $2 \times 2$  density waves are in Fig. 1 **d** with the folded BZ.

### 2D kagome lattice model: GL free energy and $M_{\text{orb}}$

The cooperation and the competition between six LC and BO order parameters,  $\boldsymbol{\eta}$  and  $\boldsymbol{\phi}$ , are well described by minimizing the Ginzburg-Landau (GL) free-energy  $F[\boldsymbol{\phi}, \boldsymbol{\eta}]$  [20, 25]; see Appendix A for its expression up to the fourth-order terms. The second-order term is  $F^{(2)} = a_b|\boldsymbol{\phi}|^2 + a_c|\boldsymbol{\eta}|^2$ , where  $a_{c(b)} = r_{c(b)}(T - T_{c(b)}^0)$ . The third-order term is  $F^{(3)} = b_1\phi_1\phi_2\phi_3 + b_2(\phi_1\eta_2\eta_3 + \eta_1\phi_2\eta_3 + \eta_1\eta_2\phi_3)$ , where the relation  $b_1 \sim -b_2$  is satisfied [20]. The fourth-order term with the coefficients  $d_1 \sim d_6$  is given in Appendix A.

When  $a_c > 0 > a_b$ , the  $3Q$  BO  $\boldsymbol{\phi}_l = \phi_l \mathbf{e}_l$  ( $l = 0, a \sim c$ ) appears alone via the first order phase transition, due to the 3rd-order  $b_1$  term. When  $a_b > 0 > a_c$ , the  $3Q$  LC  $\boldsymbol{\eta}_m = \eta_m \mathbf{e}_m$  ( $m = 0, a \sim c$ ) appears via the 2nd-order phase transition when  $d_4/2d_3 < 1$ . (In contrast, the  $1Q$  LC appears when  $d_4/2d_3 > 1$ .) When both  $a_b$  and  $a_c$  are negative, the  $3Q$ -LC  $\boldsymbol{\eta}_m$  and  $3Q$ -BO  $\boldsymbol{\phi}_l$  can coexist. For  $m \neq l$ , we obtain the  $Z_3$  nematic coexisting state shown in Fig. 1 **d**, where the centers of both orders are different (out-of-phase) [20]. This nematic state is predicted by the GL free energy analysis because of the relation  $b_1 b_2 < 0$  [20]. (The  $C_6$  coexisting state ( $m = l$ ) is energetically unfavorable for  $b_1 b_2 < 0$ .) The detailed GL free energy analysis for the LC+BO coexisting state is presented in Appendix A.

Here, we discuss how the degeneracy of the  $Z_3$  nematic states is lifted by the  $2a_0$  stripe CDW and the magnetic field. We consider the following  $Z_3$  nematic states  $(\boldsymbol{\phi}_0, \boldsymbol{\eta}_m^\pm)$  ( $m = a - c$ ) without loss of generality, where  $\boldsymbol{\phi}_0 \equiv \phi_0 \mathbf{e}_0$  and  $\boldsymbol{\eta}_m^\pm \equiv \pm \eta_m \mathbf{e}_m$  ( $\eta > 0$ ). Under the AB direction  $2a_0$  stripe that is shown in Fig. 1 **e**, the relation  $F[\boldsymbol{\phi}_0, \boldsymbol{\eta}_a] \neq F[\boldsymbol{\phi}_0, \boldsymbol{\eta}_{b(c)}]$  is realized by symmetry, considering that the director of  $(\boldsymbol{\phi}_0, \boldsymbol{\eta}_a)$  is parallel to the stripe direction. (Note that the magnitudes of  $\phi$  and  $\eta$  are almost unchanged by small  $\mathbf{B}$  and  $I_{\text{st}}$ .) Thus, the six-fold coexisting states are separated into (i) the dual state  $(\boldsymbol{\phi}_0, \boldsymbol{\eta}_a^\pm)$  at  $E = \epsilon_2$  and (ii) the quadruple state  $(\boldsymbol{\phi}_0, \boldsymbol{\eta}_{b(c)}^\pm)$  at  $E = \epsilon_4$ . (The sign of the energy difference  $\epsilon_2 - \epsilon_4$  would depend on the model parameters.)

Next, we consider the effect of the magnetic field. As we discuss in Appendix A, the orbital magnetization is expressed as  $M_{\text{orb}}[\boldsymbol{\phi}_0, \boldsymbol{\eta}_m^\pm] = \pm[-m_1\eta\phi/3 + m_2\eta^3/(3\sqrt{3}) - m_3\eta\phi^2/(3\sqrt{3})]$  for any  $m = a, b, c$ . Due to the orbital-Zeeman term  $-M_{\text{orb}}B_z$ , the energy levels of  $\boldsymbol{\eta}_m^\pm$  split, so the sign of  $\eta$  is switched by the direction of  $B_z$  while  $|\eta|$  is unchanged. The result is summarized in Fig. 1 **f**.

As we will explain later, the eMChA under the AB direction  $2a_0$  stripe CDW is proportional to the first component of the LC order;  $[\boldsymbol{\eta}_a^\pm]_1 \propto \pm\eta$  for the case (i) and  $[\boldsymbol{\eta}_{b(c)}^\pm]_1 \propto \mp\eta$  for the case (ii). Therefore, in both (i) and (ii), the eMChA is switched by the direction of  $B_z$ , which is consistent with experiments. This result is unchanged even if the GL free energy is minimized with respect to the LC order parameter  $\boldsymbol{\eta}_m = \eta \bar{\mathbf{e}}_m$ , where  $\bar{\mathbf{e}}_a \propto (a, -1, -1)$  and so on. Here,  $a (> 0)$  is a parameter given by minimizing the GL free energy;  $a \lesssim 2$  is realized for  $|\eta/\phi| \gg 1$  [20]. A more detailed explanation is presented in Appendix A.

### 3D kagome lattice model: LC stacking states

Here, we consider the three-dimensional (3D) LC state. The  $2 \times 2 \times 2$   $3Q$  LC is expressed by  $\boldsymbol{\eta} = \boldsymbol{\eta}_m$  for the first layer and the set of the inter-layer phase shifts  $\boldsymbol{\theta} = (\theta_1, \theta_2, \theta_3)$  with  $\theta_i = 0$  or  $\pi$ . Then, the second layer order is  $\boldsymbol{\eta}' = (e^{i\theta_1}\eta_1, e^{i\theta_2}\eta_2, e^{i\theta_3}\eta_3)$ . In this paper, we consider the following two cases because they are stabilized in the LC+BO coexisting state [17, 20, 25]. (1)  $\boldsymbol{\theta} = (0, 0, 0)$ , where the same 2D orders are stacked vertically, which we call the ‘‘vertical LC (v-LC)’’ state. (See Fig. 2 **e**.) (2)  $\boldsymbol{\theta} = (0, \pi, \pi)$ , where the 2D order on even-number layers and that on the odd-number layers are shifted by the vector  $\mathbf{a}_{\text{AB}}$ , which we call the ‘‘shift-stack LC (s-LC)’’ state. (See Fig. 2 **g**.) The director of the nematicity of  $\boldsymbol{\theta} = (0, \pi, \pi)$  s-LC state is along  $\mathbf{a}_{\text{AB}}$ .

Also, the  $2 \times 2 \times 2$   $3Q$  BO is expressed as  $\boldsymbol{\phi} = \boldsymbol{\phi}_0$  ( $\equiv \phi_0 \mathbf{e}_0$ ) for the first layer and the inter-layer phase shifts  $\boldsymbol{\psi} = (\psi_1, \psi_2, \psi_3)$  with  $\psi_i = 0$  or  $\pi$ . This  $3Q$  BO is stabilized by the 3rd-order  $b_1$ -term when  $b_1\phi < 0$  and  $\psi_1 + \psi_2 + \psi_3 = 0 \pmod{2\pi}$  to satisfy the momentum conservation [20].

When the LC is induced inside the 3D BO state ( $T_b^0 > T_c^0$ ), the relation  $|\phi| \gg |\eta|$  is expected. Then, the LC order  $\boldsymbol{\eta}_m = \eta \mathbf{e}_m$  ( $m = a - c$ ) is stabilized by the 3rd-order GL free energy because of the relation  $b_2 \sim -b_1 > 0$  [20]. In addition, the relation  $\boldsymbol{\psi} = \boldsymbol{\theta}$  is naturally expected (see Appendix). Thus, the v-LC (s-LC) is expected to appear inside the v-BO (s-BO) phase.

### Inversion symmetry breaking in LC+stripe state

The violation of IS is a necessary condition for the nonlinear conductivities. Here, we discuss how the IS is violated by introducing the  $2 \times 2$  LC order and the  $2a_0$  stripe CDW. The stripe CDW is generally observed in Cs-based kagome metals [44, 45].

**2D kagome lattice model:** In the original 2D kagome lattice in Fig. 2 **a**, the IS centers are given by A,

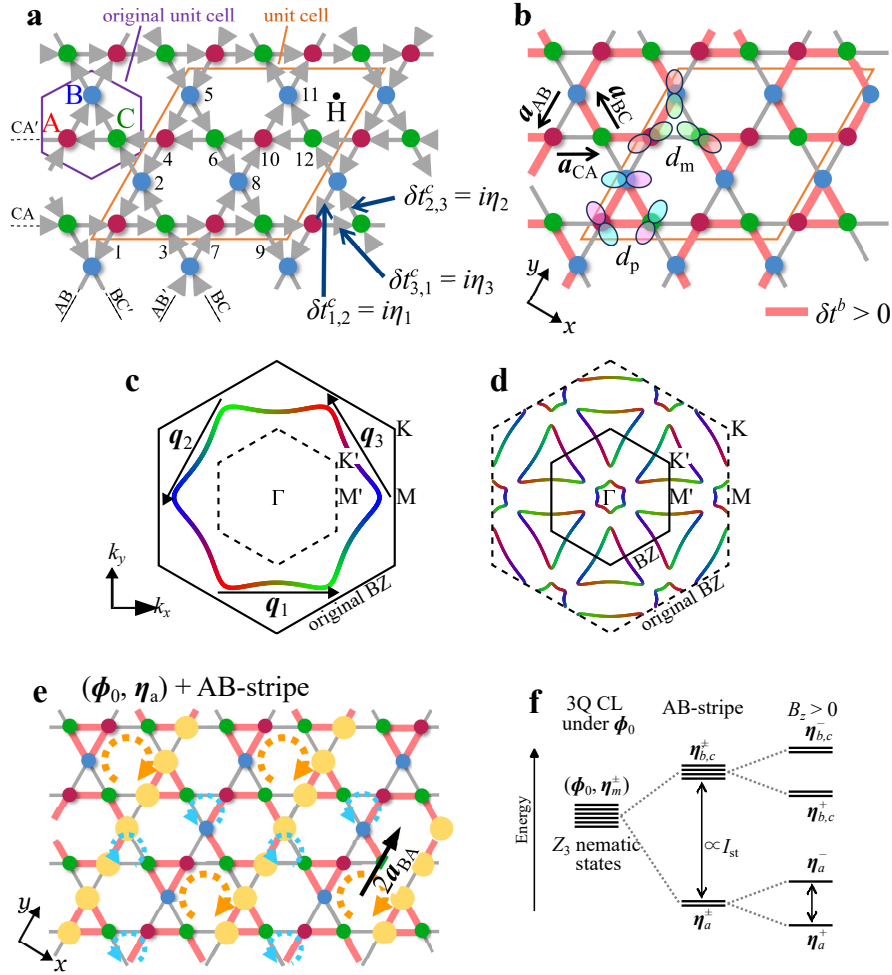


FIG. 1. **Lattice structure, FS, and BO form factor in kagome metal.** **a.** 2D kagome lattice model with  $2 \times 2$  3Q LC  $\boldsymbol{\eta} = (\eta_1, \eta_2, \eta_3)$  on  $d_p$  orbital. Note that  $(\eta_1, \eta_2, \eta_3)$  and  $(\eta_1, -\eta_2, -\eta_3)$  are the same bulk states after shifting  $\mathbf{R} = \mathbf{a}_{BC} + \mathbf{a}_{CA}$ . **b.** 3Q Tri-Hexagonal BO  $\phi = \phi_0$  ( $\phi > 0$ ) on  $d_p$  orbital. Two orbitals  $d_p$  ( $= d_{xz}$ ) and  $d_m$  ( $= d_{yz}$ ) on the V-ion are depicted. **c.** Original FSs without density waves. **d.** Folded FSs under the  $2 \times 2$  density waves with the folded BZ. **e.** Nematic LC+BO coexisting state  $(\phi_0, \boldsymbol{\eta}_a)$ , whose GL free energy is lower than the  $C_6$  LC+BO state  $(\phi_0, \boldsymbol{\eta}_0)$ . The director is parallel to  $\mathbf{a}_{AB}$ . The  $2a_0$  stripe CDW along AB direction is shown by the yellow circles. **f.** Lift of the six-fold degenerated nematic states  $(\phi_0, \boldsymbol{\eta}_m^\pm)$  ( $m = a, b, c$ ) due to the stripe potential and the magnetic field. Here,  $\boldsymbol{\eta}_m^\pm \equiv \pm|\eta|e_m$ .

B, C, and H, which are denoted by filled square symbols. Note that H is the center of the  $C_6$  rotational symmetry. When the 3Q LC order is introduced, only the inversion center H survives as shown in Fig. 2 b. Note that the inversion center H survives even if the 3Q-LC and 3Q-BO coexist, in both in-phase ( $C_6$  symmetry) and out-of-phase ( $C_2$  symmetry) states [20]. Thus, IS is not violated by 3Q-LC and 3Q-BO. We stress that IS is broken by introducing the  $2a_0$  stripe CDW, as we show in Fig 2 c. Here, the yellow circles represent the stripe CDW potentials  $I_{st}$ , which is consistent with the energy-independent (vertical) QPI signal with period  $2a_0$  observed in Ref. [44, 45]. Hereafter, we analyze only the  $2a_0$  stripe CDW in the numerical study. (The IS is also violated by introducing the period  $4a_0$  CDW, while stripe CDW alone does not break the IS.)

**3D kagome lattice model:** In the original 3D crystal structure shown in Fig. 2 d, the IS centers are described by A, B, C, H (filled square symbols), and A', B', C', H' (open square symbols). Here, X' are the middle points between two layers. Figure 2 e shows a v-LC state with  $\boldsymbol{\theta} = (0, 0, 0)$ . Here, only the IS centers H and H' survive as shown in Fig. 2 e. In Fig. 2 f, we introduce the  $2a_0$  stripe CDW. Then, none of the IS centers remains as we show in Fig. 2 f. Then, we find that the eMChA becomes finite. Figure 2 g shows the s-LC state with  $\boldsymbol{\theta} = (0, \pi, \pi)$ . Here, the 3Q LC on the even-number layers and that on the odd-number layers are shifted by the vector  $\mathbf{a}_{AB}$ . In this  $2 \times 2 \times 2$  s-LC state, only the IS center C' survives as shown in Fig. 2 g. By introducing the  $2a_0$  stripe CDW along AB direction, none of the IS centers remain as we show in Fig. 2 h. Then, we find

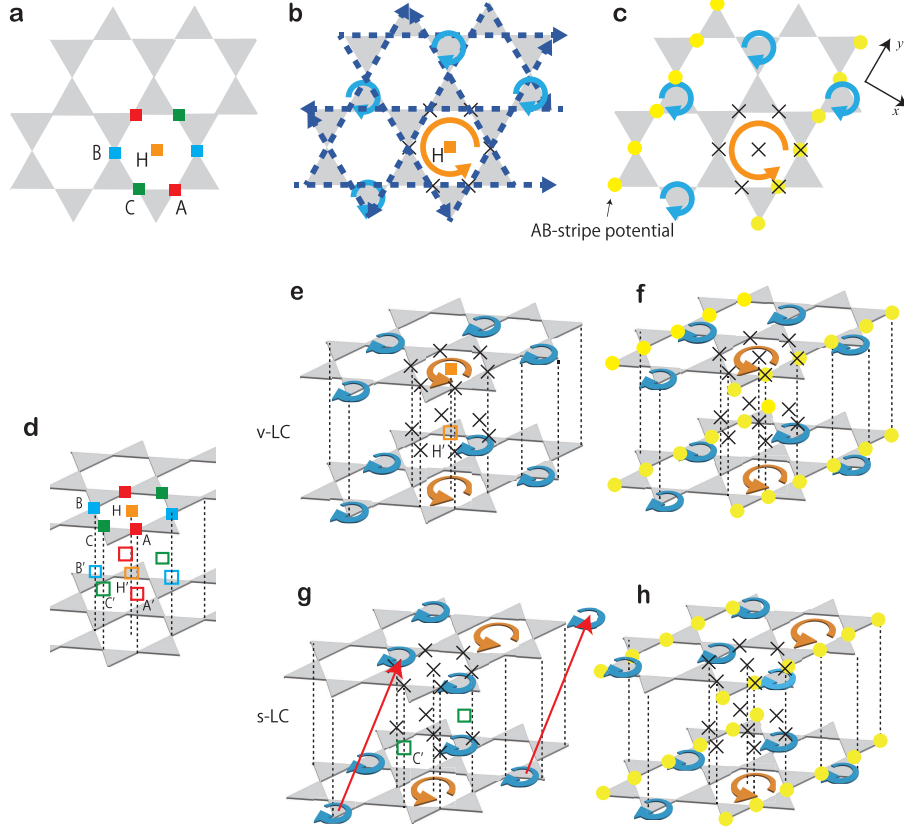


FIG. 2. **Inversion symmetry breaking in LC+stripe state.** **a.** Original 2D crystal structure. The IS centers are described by A, B, C, H. **b.**  $2 \times 2$  LC order with remaining IS center H. **c.** Coexisting phase of  $2 \times 2$  LC and  $2a_0$  stripe CDW. Thus, IS is broken when the LC and stripe CDW coexist. **d.** Original 3D crystal structure. The IS centers are described by A, B, C, H, A', B', C', H'. **e.** v-LC with remaining IS centers H and H'. **f.** Coexisting phase of v-LC and  $2a_0$  stripe CDW. In this case, the IS is broken. **g.** s-LC with remaining IS center C'. **h.** Coexisting phase of s-LC and  $2a_0$  stripe CDW, where the shift-stacking direction and the stripe direction are parallel. In this case, the IS is broken.

that the eMChA becomes finite. Note that the IS center C' remains intact if the  $2a_0$  stripe CDW is along BC or CA directions, and therefore the eMChA disappears.

To summarize, by introducing the  $2a_0$  stripe CDW that is generally observed in Cs-based compounds, the IS is broken in both the v-LC state in Fig. 2 f ( $\theta = (0, 0, 0)$ ) and the s-LC state in Fig. 2 h ( $\theta = (0, \pi, \pi)$ ). In both cases, finite eMChA is expected to be realized. (In contrast, the alternative v-LC state with  $\theta = (\pi, \pi, \pi)$  preserves the IS even after introducing the stripe, so the eMChA vanishes.) It is noteworthy that the IS in the 1Q-LC state is broken by introducing the stripe CDW that is parallel to the 1Q-LC order. Therefore, giant eMChA conductivity can be realized in the 1Q-LC states.

### NLH and eMChA conductivities

In this section, we study the second-order response to

the electric field  $\mathbf{E}$  in the LC state in kageme metals. The nonlinear Hall conductivity  $\sigma_{\alpha\beta\beta'}$  is defined as

$$\Delta j_\alpha = \sigma_{\alpha\beta\beta'} E_\beta E_{\beta'} \quad (3)$$

where  $j_\alpha$  is the charge current along the  $\alpha$ -axis of order  $O(E^2)$ . Here,  $\alpha, \beta, \beta' = x, y, \text{ or } z$ . The eMChA conductivity  $\sigma_{\alpha\beta\beta',\gamma}$  is defined as

$$\Delta j_\alpha = \sigma_{\alpha\beta\beta',\gamma} E_\beta E_{\beta'} B_\gamma \quad (4)$$

where  $B_\gamma$  is the magnetic field along the  $\gamma$  axis. Under the inversion operation,  $\Delta \mathbf{j}$  and  $\mathbf{E}$  are reversed while  $\mathbf{B}$  is unchanged. In addition,  $\sigma_{\alpha\beta\beta'}$  and  $\sigma_{\alpha\beta\beta',\gamma}$  are unchanged if the system is centrosymmetric. Therefore,  $\sigma_{\alpha\beta\beta'} = \sigma_{\alpha\beta\beta',\gamma} = 0$  in any centrosymmetric system. Thus, the IS breaking is a necessary condition for the finite  $\sigma_{\alpha\beta\beta'}$  and  $\sigma_{\alpha\beta\beta',\gamma}$ . Here, the eMChA coefficient is given as  $\gamma_{eM} \equiv -\sigma_{zzz,x}/(\sigma_{zz})^2$ .

Under the time-reversal operation, the signs of  $\Delta \mathbf{j}$  and  $\mathbf{B}$  are reversed. For this reason, the eMChA (NLH) conductivity is  $T$ -even ( $T$ -odd). Thus, the  $\eta$ -linear eMChA

is proportional to  $\eta\tau^{2n+1}$ . Also, the  $\eta$ -linear NLH is proportional to  $\eta\tau^{2m}$ . We find that the highest term with respect to  $\tau$ , which gives the most divergent contribution in good metals, is  $\eta\tau^3$  ( $\eta\tau^2$ ) for the eMChA (NLH) due to the chiral LC order.

In Appendix C, we derive the most divergent linear and nonlinear conductivities with respect to the  $\tau$  based on the relaxation time approximation. The derived formulae are given as

$$\sigma_{\alpha\alpha} = -e^2 \frac{g_s}{N} \sum_{a,\mathbf{k}} (f' v^\alpha v^\alpha)_{a,\mathbf{k}} \frac{1}{2\gamma} \quad (5)$$

$$\sigma_{\alpha\beta\beta} = e^3 \frac{g_s}{N} \sum_{a,\mathbf{k}} (f' v^\beta v^{\alpha\beta})_{a,\mathbf{k}} \frac{1}{4\gamma^2}, \quad (6)$$

$$\begin{aligned} \sigma_{\alpha\beta\beta,\gamma} &= e^4 \frac{g_s}{N} \sum_{a,\mathbf{k}} \epsilon^{\gamma\phi\eta} (-f' v^{\alpha\beta} v^{\beta\eta} v^\phi)_{a,\mathbf{k}} \frac{1}{4\gamma^3} \\ &+ \Delta\sigma_{\alpha\beta\beta,\gamma}, \end{aligned} \quad (7)$$

where  $\gamma = 1/2\tau$  is the quasiparticle (QP) damping rate,  $f'$  is the  $\epsilon$ -derivative of Fermi distribution function,  $g_s = 2$  is the spin degeneracy, and  $\epsilon^{\alpha\beta\gamma}$  is Levi-Civita symbol. Here,  $\Delta\sigma_{\alpha\beta\beta,\gamma} \equiv e^4 \frac{g_s}{N} \sum_{a,\mathbf{k}} \epsilon^{\gamma\phi\eta} (f' v^{\alpha\eta} v^{\beta\phi} v^\beta)_{a,\mathbf{k}} \frac{1}{8\gamma^3}$ , which vanishes when  $\alpha = \beta$ . According to the TABLE I, the NLH in the present model is finite for  $\sigma_{y\mu\mu}$  ( $\mu = x, y, z$ ). Also, the eMChA is finite for  $\sigma_{z\mu\mu,x}$  and  $\sigma_{x\mu\mu,z}$ .

In the numerical study, we derive  $v_{a,\mathbf{k}}^{\alpha\beta} \equiv \partial_\alpha \partial_\beta \epsilon_{a,\mathbf{k}}$  from the sum rule  $v_{a,\mathbf{k}}^{\alpha\beta} = \tilde{v}_{a,\mathbf{k}}^{\alpha\beta} + 2g_{a,\mathbf{k}}^{\alpha\beta}$ . Here,  $\tilde{v}_{a,\mathbf{k}}^{\alpha\beta} \equiv \langle u_{a,\mathbf{k}} | (\partial_\alpha \partial_\beta \hat{H}_{\mathbf{k}}^0) | u_{a,\mathbf{k}} \rangle$ , and  $g_{a,\mathbf{k}}^{\alpha\beta}$  is given by

$$g_a^{\alpha\beta} = \frac{1}{2} \sum_{b \neq a} \frac{\text{Re}[v_{ab}^\alpha v_{ba}^\beta + v_{ab}^\beta v_{ba}^\alpha] \epsilon_{ab}}{\epsilon_{ab}^2 + \delta^2}, \quad (8)$$

where  $\delta = 0$  corresponds to the sum rule for the free-electron, while we introduce  $\delta = 0.001$  to obtain reliable numerical results. ( $\delta$  would correspond to  $\text{Im}\Sigma^A$ .) Note that Eq. (8) is derived from the covariant differential of the operator  $v^z = \partial_z H^0$ :  $D_z v^z = \partial_z v^z - i[A^z, v^z]$ , where  $A_{a,b}^z = i\langle u_a | \partial_z u_b \rangle$  is the Berry connection. We call  $g_a^{\alpha\beta}$  as the quasi-quantum metric (qQM) of the Bloch wavefunction because of its close relationship to the quantum metric (QM) given by

$$G_a^{\alpha\beta} = \sum_{l \neq n} \frac{\text{Re}[v_{ab}^\alpha v_{ba}^\beta + v_{ab}^\beta v_{ba}^\alpha]}{\epsilon_{ab}^2 + \delta^2}, \quad (9)$$

where  $g_a^{\alpha\beta}$  and  $G_a^{\alpha\beta}$  differ in the power in  $\epsilon_{ab}$  in the denominator. In particular, both qQM and QM take huge values when the conduction and valence bands are nearly degenerated. In later sections, we find that the giant eMChA conductivity in kagome metal is caused by the  $\eta$ -odd part of the QM ( $G^{zz,-}$ ) at the Fermi level, which gives a resonantly enhanced contribution for  $\eta \lesssim 0.02$ .

### $d_p + d_m$ orbital 3D kagome metal model: Dipole potential and quasi-Quantum Metric.

To perform a semi-quantitative analysis of the nonlinear conductivities in kagome metals, we introduce a 3D kagome lattice model with  $d_p$  and  $d_m$  orbitals. In kagome metals, the  $d_p$  ( $d_m$ ) orbital gives the pure-type (mix-type) FS with a narrower (wider) bandwidth. The FSs of the present 3D kagome metal are shown in Fig. 3 **a** for the electron filling at  $n_{\text{exp}} = 4.6$ . The  $d_p$  orbital weight is expressed as red color. These FSs are qualitatively consistent with the main FSs of the first-principles DFT calculation for CsV<sub>3</sub>Sb<sub>5</sub>, which are shown by brown dotted lines. The model parameters and the bandstructure are explained in Appendix B. Here, we introduce the inter-layer hopping integrals for  $d_m$  orbital to reproduce the  $k_z$ -dependence of the vHS energy of the mix-type band [76, 77].

Both pure-type and mix-type FSs are very close in energy and these two  $d$ -orbital characters are mixed on the FSs. Therefore, the  $2 \times 2$  LC order on the  $d_p$  orbitals ( $\eta$ ) causes prominent pure-mix band hybridization and the FS reconstruction. This fact causes large  $M_{\text{orb}}$  in the LC phase [25]. The pure-mix band reconstruction gives rise to the giant eMChA in kagome metals, as we will explain below.

We further introduce the  $2a_0$  stripe CDW potential  $I_{\text{st}}$ , which is consistent with the dispersionless (vertical) QPI signal for the stripe [44, 45]. As we explained above, the inversion symmetry is violated when  $\eta I_{\text{st}} \neq 0$ . Then, the inversion symmetry of the band dispersion  $\epsilon_{b,\mathbf{k}}$  is broken, *i.e.*,  $\epsilon_{b,\mathbf{k}} \neq \epsilon_{b,-\mathbf{k}}$ . In this paper, we denote the  $\eta$ -odd and  $\eta$ -even parts of the function  $X$  as  $X^-$  and  $X^+$ , respectively. They are defined as  $X^\pm \equiv ([X]_\eta \pm [X]_{-\eta})/2$ . In the present system, the relation  $\epsilon_{b,\mathbf{k}}^\pm = \pm \epsilon_{b,-\mathbf{k}}^\pm$  is satisfied. That is,  $\epsilon_{b,\mathbf{k}}^-$  is an odd-function of  $\mathbf{k}$ , because time-reversal operation gives  $\mathbf{k} \rightarrow -\mathbf{k}$  and  $\eta \rightarrow -\eta$ . Figure 3 **b** shows the numerical result of  $\epsilon_{b,\mathbf{k}}^-$  ( $b = 9$ ) under the AB stripe CDW for  $\eta = 0.05$ .  $\epsilon_{b,\mathbf{k}}^-$  give a ‘‘dipole potential in  $\mathbf{k}$ -space’’ because it is proportional to  $k_y$ . It has the symmetry-protected nodes on the  $k_x$ -axis line and other two nodes on  $k_y \approx \pm\sqrt{3}k_x$  line. Its schematic picture is given in Fig. 3 **c**.

Now, we consider the symmetry of the  $3Q$  LC order depicted in Fig. 1 **a** and Fig. 2 **b**. The kagome lattice belongs to the  $D_{6h}$  point group. Around point  $H$ , the LC pattern preserve the IS, while all the parities of the six mirror operations along the  $\theta = (\pi/6)m$  axis ( $m = 0, 1, \dots, 5$  for  $3\sigma_h$  and  $3\sigma_v$ ) are  $-1$ . Thus, the LC order belongs to the  $A_{2g}$  irreducible representation, whose basis function is  $x(x^2 - 3y^2)y(3x^2 - y^2)$ . Also, the AB direction stripe CDW changes its sign under  $k_y \rightarrow -k_y$  ( $M_y$  mirror), while it is unchanged under  $k_x \rightarrow -k_x$  ( $M_x$  mirror). Based on the second-order perturbation theory, the derived ( $\eta I_{\text{st}}$ )-linear energy shift  $\epsilon_{\mathbf{k}}^-$  is odd (even) for  $M_y$  ( $M_x$ ) mirror. The obtained dipole potential  $\epsilon_{\mathbf{k}}^- \propto k_y \eta I_{\text{st}}$

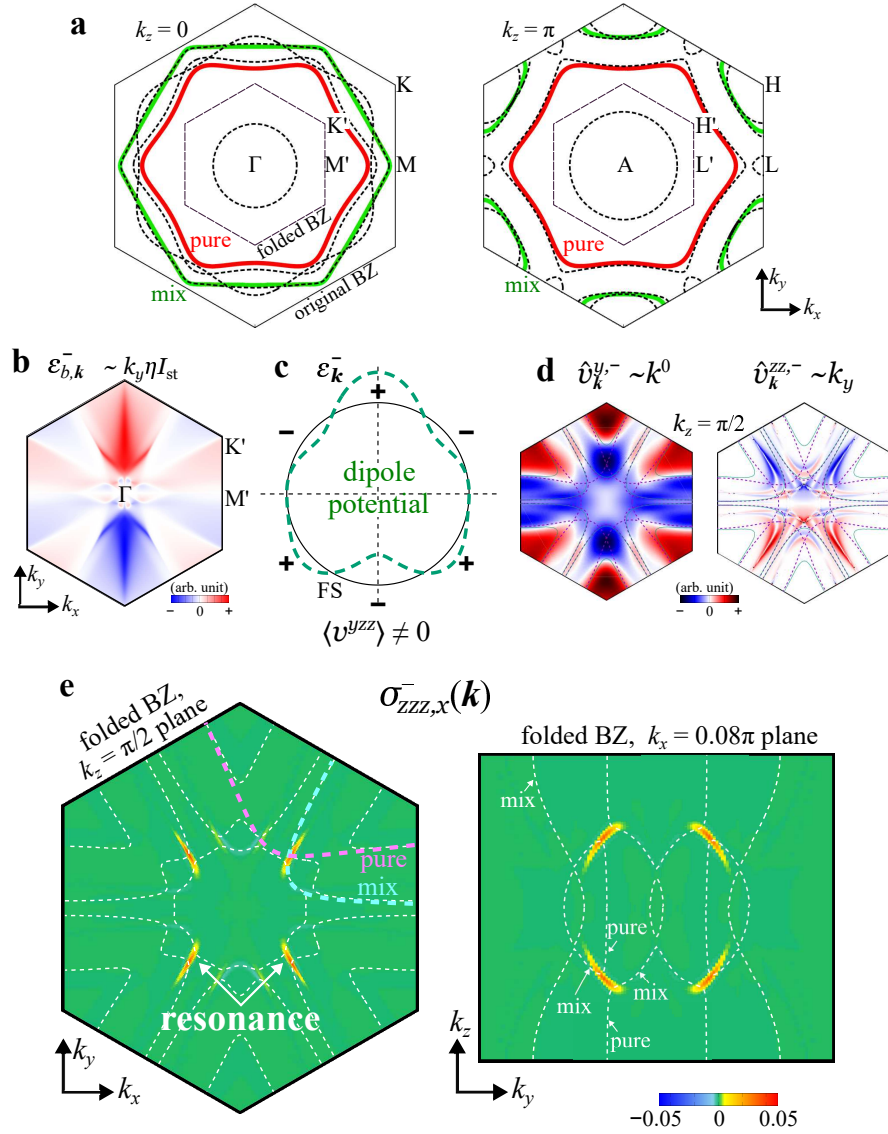


FIG. 3. **eMChA due to dipole potential and qQM-induced enhancement.** **a.** FSs of the  $d_p + d_m$  orbital 3D kagome lattice model in the original BZ. The  $d_p$  orbital weight is expressed as red color. These FSs qualitatively fit the main FSs of the first-principles DFT calculation (brown dotted lines). **b.** Dipole potential  $\epsilon_{b,\mathbf{k}}^- \sim k_y \eta I_{st}$  in the folded BZ for  $\eta = 0.05$  and  $I_{st} = 0.01$ . **c.** Schematic picture of the dipole potential. It gives no macroscopic current ( $\langle v \rangle = \mathbf{0}$ ) because of the Bloch's theorem. However, it gives finite  $\langle v^{yzz} \rangle$ . Then, the NLH  $\sigma_{yzz}$  and the eMChA  $\sigma_{zzz,x}$  becomes finite. **d.**  $\hat{v}_{\mathbf{k}}^{y,-} \sim k^0$  and  $\hat{v}_{\mathbf{k}}^{zz,-} \sim k_y$  in the folded BZ. They originate from  $\epsilon_{b,\mathbf{k}}^-$  in **b.** **e.**  $\sigma_{zzz,x}^-(\mathbf{k})$  on  $k_z = \pi/2$  plane and  $k_x = 0.08\pi$  plane for  $\eta = 0.024$  and  $I_{st} = 0.01$  at  $T = 0.01$ . It is an even function of  $\mathbf{k}$ , so its  $\mathbf{k}$  summation remains finite.

corresponds to Figs. 3 **b** and **c**.

Here, we consider  $v_{b,\mathbf{k}}^{\mu,\pm} = \partial_{\mu} \epsilon_{b,\mathbf{k}}^{\pm}$  and  $v_{b,\mathbf{k}}^{\mu\nu,\pm} = \partial_{\mu} \partial_{\nu} \epsilon_{b,\mathbf{k}}^{\pm}$ . Then,  $v_{b,\mathbf{k}}^{\mu,-}$  is even-parity and  $v_{b,\mathbf{k}}^{\mu\nu,-}$  is odd-parity. These facts give rise to the  $B_z$ -tunable nonreciprocal conductivities. Figure 3 **d** shows the obtained  $\hat{v}_{\mathbf{k}}^{y,-}$  and  $\hat{v}_{\mathbf{k}}^{zz,-}$  on the  $k_z = \pi/2$  plane in the folded BZ. Here, the average around the Fermi level is taken as  $\hat{v}_{\mathbf{k}}^{\Sigma} \equiv \sum_b v_{b,\mathbf{k}}^{\Sigma} (-f'(\epsilon_{b,\mathbf{k}}))$  ( $\Sigma = y, -$  or  $zz, -$ ). Note that  $f'(0) = -1/4T$ . The symmetries of  $v_{b,\mathbf{k}}^{\mu,\pm}$  and  $v_{b,\mathbf{k}}^{\mu\nu,\pm}$  are summarized in Table I. This table is useful to understand what kinds of nonreciprocal conductivities become

finite. (Note that Figs. 3 **b** and **d** exhibit moderate  $\mathbf{k}$ -dependence because we set larger  $\delta, \eta, T = 0.05$ , where the qQM term is less important.)

Now, we present an intuitive explanation why the NLH and eMChA conductivities emerge in the LC state with the AB direction stripe CDW. First, we consider the averaged current  $\langle v^y \rangle \propto \sum_{\mathbf{k}} v^y f$ , where  $f$  the Fermi distribution function, which is expanded as  $f(\epsilon_{\mathbf{k}}) \approx f(\epsilon_{\mathbf{k}}^+) + f'(\epsilon_{\mathbf{k}}^+) \epsilon_{\mathbf{k}}^-$  with respect to the dipole potential. One may consider that  $\langle v^y \rangle$  becomes finite because  $v_{\mathbf{k}}^{y,+} \epsilon_{\mathbf{k}}^-$  is even with respect to  $M_x$  and  $M_y$ . However,  $\langle v^y \rangle$  is exactly

TABLE I. **a.**  $\mathbf{k}$ -dependences of  $v^{\mu,\pm}$  and  $\Omega^{\mu,\pm}$ , and **b.**  $\mathbf{k}$ -dependences of  $v^{\mu\nu,\pm}$  in the LC state with AB-stripe CDW. Note that each function in the table should be multiplied by an  $A_{1g}$  (totally symmetric) function in taking the derivative.

$\mu =$	$x$	$y$	$z$
$v^{\mu,-}$	$k_x k_y$	1	$k_y k_z$
$v^{\mu,+}$	$k_x$	$k_y$	$k_z$
$\Omega^{\mu,-}$	$k_x k_z$	$k_y k_z$	1
$\Omega^{\mu,+}$	$k_x k_y k_z$	$k_z$	$k_y$

$\mu\nu =$	$xx, yy$	$zz$	$xz$	$yz$	$xy$
$v^{\mu\nu,-}$	$k_y$	$k_y$	$k_x k_y k_z$	$k_z$	$k_x$
$v^{\mu\nu,+}$	1	1	$k_x k_z$	$k_y k_z$	$k_x k_y$

zero because the present LC order is periodic in the  $2 \times 2$  unit cell, known as the Bloch's theory based on the Galilean transformation argument [78]. This is also simply proved as  $\langle \mathbf{v} \rangle \propto \sum_{\mathbf{k}} \mathbf{v} f(\epsilon_{\mathbf{k}}) = \sum_{\mathbf{k}} \nabla_{\mu}(\epsilon_{\mathbf{k}} - \mu) f(\epsilon_{\mathbf{k}}) = -\sum_{\mathbf{k}} (\epsilon_{\mathbf{k}} - \mu) f'(\epsilon_{\mathbf{k}}) \mathbf{v} = \mathbf{0}$  at  $T = 0$ .

Here, we discuss the linear conductivity and the NLH conductivity for  $\mathbf{B} = \mathbf{0}$  defined as  $j_z = \sigma_{zz} E_z$  and  $j_y = \sigma_{yz} E_z^2$ , respectively. The linear conductivity of order  $O(\tau^1)$  is  $\sigma_{zz} \propto \langle v^{zz} \rangle \gamma^{-1}$  ( $v^{zz} \equiv \partial_z v^y$ ), which is easily derived from Eq. (5) by using the integration by parts. Also, the NLH conductivity of order  $O(\tau^2)$  is given as  $\sigma_{yz} \propto \langle v^{yzz} \rangle \gamma^{-2}$  ( $v^{yzz} \equiv \partial_y v^{zz}$ ), which is derived from Eq. (6) directly. We understand that  $\langle v^{yzz} \rangle$  is finite because the  $\eta$ -odd term  $v^{yzz,+} \epsilon_{b,\mathbf{k}}^-$  has even-parity and there is no accidental cancellation. (The Bloch's theory [78] does not prohibit the finite  $\langle v^{yzz} \rangle$ .) In this case, in the presence of  $B_x$ , finite  $\langle v^z \rangle$  appears due to the Lorentz force. Thus, TRS breaking dipole potential  $\epsilon_{\mathbf{k}}^-$  gives finite NLH and eMChA conductivities.

Finally, we demonstrate the important role of the resonantly enhanced qQM for smaller  $\eta$  and  $\delta$ . Let  $\sigma_{zz,x}^-(\mathbf{k})$  be the  $\eta$ -odd part of the function under integration in Eq. (7). Figure 3 e shows  $\sigma_{zz,x}^-(\mathbf{k})$  on the  $k_z = \pi/2$  and  $k_x = 0.08\pi$  planes for  $\eta = 0.024$  and  $I_{\text{st}} = 0.01$  at  $T = 0.01$ . It exhibits resonant-like sharp peaks around the position where the pure-mix band reconstruction occurs under the LC order. The pure-type and mix-type FSs at  $\eta \neq 0$  are drawn in Figure 3 e, and their original FSs at  $\eta = 0$  are expressed in Fig. S1 in the folded BZ. Around this ‘‘resonant positions’’, the mixture of the LC order ( $\eta$ ) in the pure-band and the large  $k_z$ -direction dispersion in the mix-band gives rise to large  $g_{zz,-}^{zz,+} g_{zz,+}^{zz,-}$  ( $\propto 1/|\eta|$ ). Thus, giant eMChA comes from the square of qQM that are resonantly magnified by the ‘‘pure-mix band reconstruction’’ in the LC phase. ( $\sigma_{zz,x}^+(\mathbf{k})$  vanishes after the  $\mathbf{k}$  summation because of the relations  $g_{\mathbf{k}}^{\pm} = \pm g_{-\mathbf{k}}^{\pm}$  and  $G_{\mathbf{k}}^{\pm} = \pm G_{-\mathbf{k}}^{\pm}$ .)

## Numerical study of NLH and eMChA conductivities for v-LC and s-LC states

Here, we perform the numerical study of the nonlinear conductivities in the v-LC and s-LC states, under the stripe CDW along the AB direction (along the  $y$ -axis). We put  $\eta = 0.008 - 0.024$ ,  $I_{\text{st}} = 0.01$  and  $T = 0.01$  in the energy unit eV. The obtained eMChA are almost unchanged for  $T = 0.005$ . To achieve enough numerical accuracy, we use  $480 \times 480 \times 240$   $\mathbf{k}$ -meshes in the original BZ. The obtained eMChA is essentially unchanged even when  $240 \times 240 \times 120$   $\mathbf{k}$ -meshes are used. We set  $\gamma = 1$ ,  $e = 1$  and  $\hbar = 1$  for simplicity.

Figures 4 a and b show the eMChA conductivity  $\sigma_{zzz,x}$  and the NLH conductivity  $\sigma_{yxx}$  in the v-LC state,  $\boldsymbol{\eta} = \eta \mathbf{e}_a$  and  $\boldsymbol{\psi} = (0, 0, 0)$ , as functions of the electron filling  $n$  at  $T = 0.01$ . (The obtained results are essentially unchanged for  $T = 0.001 \sim 0.01$ .)  $n_{\text{exp}}$  corresponds to the electron filling of  $\text{CsV}_3\text{Sb}_5$ , and  $n_{\text{vHS}}$  is the vHS filling for the  $d_p$ -orbital band. Both  $\sigma_{zzz,x}$  and  $\sigma_{yxx}$  are odd-functions of  $\eta$ , so they are reversed by changing the direction of  $B_z$ . Unexpectedly,  $\sigma_{zzz,x}$  increasing with decreasing the LC order for  $\eta \geq 0.008$ , and  $\sigma_{yxx}$  is nearly independent of  $\eta$ . The same behaviors are obtained for  $\eta = 0.008 \sim 0.064$ ; see Appendix D. Both  $\sigma_{zzz,x}$  and  $\sigma_{yxx}$  significantly decrease if the  $v_{b,\mathbf{k}}^{\mu\nu}$  in Eqs. (6) and (7) is replaced with  $\tilde{v}_{b,\mathbf{k}}^{\mu\nu}$ , that is, if the the qQM  $g_{b,\mathbf{k}}^{\mu\nu}$  is dropped. Therefore, giant nonreciprocal conductivities originate from the qQM term, which is drastically enlarged near the band crossing points.

Considering that the LC transition temperature  $T_{\text{LC}}$  reported in kagome metals is  $35 \sim 130\text{K}$ , the magnitude of the order parameter at  $T = 0$  will be  $|\boldsymbol{\eta}| = 0.005 \sim 0.02$  [eV] in the case of  $|\boldsymbol{\eta}|/T_{\text{LC}} \sim 2$ . Therefore, giant eMChA observed in kagome metals is given by the resonantly magnified QM term. In Appendix D, we find that  $\sigma_{zzz,x}$  and  $\sigma_{yxx}$  in the v-LC state in Fig. 4 a and b are almost unchanged in the s-LC state. They are qualitatively unchanged if the  $2 \times 2$  LC and BO coexist.

In Appendix E, we recover the unit of the conductivities given by the numerical study in Fig. 4 and Fig. S3 f. We obtain  $\rho_{zz}^{\text{exp}} \approx 40000\gamma$  [ $\mu\Omega\text{cm}$ ] and  $\rho_{xx}^{\text{exp}} = 2500\gamma$  [ $\mu\Omega\text{cm}$ ]. Considering the experimental values  $\rho_{zz} \approx 30$  [ $\mu\Omega\text{cm}$ ] [29] and  $\rho_{xx} = 0.4$  [ $\mu\Omega\text{cm}$ ] [11], we expect that  $\gamma \lesssim 1 \times 10^{-3}$  [eV] in high-quality kagome metals for  $T \lesssim 5\text{K}$ . By calculating  $\gamma_{\text{eM}} = -\sigma_{zzz,x}/(\sigma_{zz})^2$  numerically, we obtain  $|\gamma_{\text{eM}}| \sim G/\gamma$ , where  $G \sim 20 \cdot (100I_{\text{st}}[\text{eV}])$  for  $\eta \sim 0.008$  and  $n \approx n_{\text{exp}}$ . Its unit is recovered as  $|\gamma_{\text{eM}}^{\text{exp}}| \sim 10^{-17} \cdot (100I_{\text{st}}/\gamma) [A^{-1}T^{-1}m^2]$ . Under finite  $B_x$  measurement, the eMChA coefficient is magnified by the factor  $z^2$ , where  $z \equiv \frac{\rho_{zz}(B_x)}{\rho_{zz}(0)}$ . In kagome metals,  $z \sim 20$  for  $B_x = 18\text{T}$  [29].

In addition, we discuss the eMChA coefficient by using the numerical result of  $\sigma_{zzz,x}$  in Fig. 4 a and the



experimental resistivity  $\rho_{zz}(18\text{T}) \sim 500 [\mu\Omega\text{cm}]$  [29]. In Fig. 4 **a**,  $\sigma_{zzz,x} \sim 2 \times 10^{-4}$  for  $\eta \sim 0.008$  and  $I_{\text{st}} \sim 0.01$  at  $n \sim n_{\text{exp}}$ . Then, the unit is recovered as  $|\gamma_{\text{eM}}^{\text{exp}}| \sim 10^{-12}/(\gamma [\text{eV}])^3 [A^{-1}T^{-1}m^2]$ . Thus, experimental giant eMChA coefficient  $\gamma_{\text{eM}}^{\text{exp}} \sim 10^{-11} [A^{-1}T^{-1}m^2]$  can be understood by putting  $\gamma \lesssim 10^{-3} [\text{eV}]$  and  $I_{\text{st}} \sim 0.01 [\text{eV}]$  in the present theory.

We also calculate  $M_{\text{orb}}$  and the anomalous Hall conductivity  $\sigma_{xy}^{\text{AHE}}$  for  $\eta = 0.008$  as functions of  $n$  in Fig. 4 **c**. (Here, the unit of the vertical axis is arbitrary.) Both  $M_{\text{orb}}$  and  $\sigma_{xy}^{\text{AHE}}$  changes their signs for  $\eta \rightarrow -\eta$ . These quantities take large values for  $n \approx n_{\text{exp}}$ , and their absolute values become maximum for  $n \approx n_{\text{vHS}}$ ,

Figure 4 **d** shows  $\sigma_{zzz,x}$ ,  $\sigma_{yzz}$ ,  $M_{\text{orb}}$ , and  $\sigma_{xy}^{\text{AHE}}$  in an arbitrary unit as functions of  $\eta$ . We set  $n = 4.8$  to avoid the exceptional  $\eta$ -dependence of  $\sigma_{yxx}$  at  $n = n_{\text{exp}}$  shown in Fig. 4 **b**. Here, we introduce the small BO  $\phi = 0.004$  to make the numerical calculation stable for  $\eta \sim 0$ . We find that only  $\sigma_{zzz,x}$  exhibits the resonance-like singular behavior  $\propto \eta^{-1}$  for  $\eta \gtrsim 0.005$ . Importantly, this resonance-like behavior appears for a wide range of  $n$ . (Although the maximum of  $\sigma_{zzz,x}$  at  $\eta \equiv \eta_{\text{max}}$  decreases with  $\phi$ , the value of  $\eta_{\text{max}} \approx 0.005$  is essentially independent of  $\phi$ ; see Fig. S3 **d**.) In Fig. 4 **d**,  $M_{\text{orb}} \propto \eta$  for  $\eta \ll 0.01$  due to the  $\eta$ - $\phi$  bilinear term in  $M_{\text{orb}}$ ; see Appendix A. However,  $M_{\text{orb}} \propto \eta^3$  is realized for  $\eta \gtrsim 0.01$ .

Here, we discuss the close relation between the eMChA and the QM. We find that the eMChA is approximately given as  $\sigma_{zzz,x} \sim \sum_{a,\mathbf{k}} \epsilon^{x\eta\phi} [f'v^{\phi,+}(v^{zz}v^{\eta z})^-]_{a,\mathbf{k}}$ . Considering a  $(a,b)$ -band model, the relation  $(v^{zz}v^{zz})_a^- \approx (g^{zz}g^{zz})_a^- \approx 2G_a^{zz,-} \cdot (v_{ab}^z v_{ba}^z)_a^+$  is realized. Thus, the resonance-like behavior of  $\sigma_{xxx,z}$  in Fig. 4 **d** originates from  $G^{zz,-} \sim (v^{z,+})^3 (v^{z,-})_{ab}^{-2} \sim \eta^{-1}$  near the resonant positions. Figure 4 **e** shows the  $\eta$ -odd part of the QM at the Fermi level,  $G_{\mathbf{k}}^{zz,-} = \sum_a G_{a,\mathbf{k}}^{zz,-} (-f'(\epsilon_{a,\mathbf{k}}^0))$ , on the  $\mathbf{k}_z = \pi/2$  plane. Its peak positions are almost the same as those of  $\sigma_{zzz,x}(\mathbf{k})$  shown in Fig. 3 **e**. Thus, both quantities are magnified by the ‘‘pure-mix band reconstruction’’ caused by the  $2 \times 2$  LC, owing to the finite  $d_p$ -orbital weight on the mix-type FS. In addition, the  $d_m$ -orbital inter-layer hopping  $t_{m\perp}$  is necessary for finite  $G_{\mathbf{k}}^{zz,-}$ . Therefore, the giant eMChA in kagome metal originate from the  $\eta$ -odd QM  $G_{\mathbf{k}}^{zz,-}$ . In contrast, the NLH does not exhibit the resonance-like behavior as shown in Fig. 4 **d**, because the qQM  $g_{a,\mathbf{k}}^{\mu\nu}$  in  $\sigma_{yzz} \sim \sum_{a,\mathbf{k}} (f'v^z v^{yz})_{a,\mathbf{k}}$  drastically changes its sign around the FSs as functions of  $(a, \mathbf{k})$ , and its contributions are cancelled out upon the  $\mathbf{k}$  integration. In Appendix F, we demonstrate the relations  $v_{\mathbf{k}}^{z,-} \approx g_{\mathbf{k}}^{zz,-}$  and  $((g^{zz})_{\mathbf{k}}^-)^2 \propto G_{\mathbf{k}}^{zz,-}$ , both of which show peak structure around the resonant positions. We find that  $v_{\mathbf{k}}^{z,-}$  exhibits the sudden sign changes near the resonant position. In contrast,  $G_{\mathbf{k}}^{zz,-}$  do not show a sign change across the FS: It is essentially positive (negative) for  $k_y > 0$  ( $k_y < 0$ ). Therefore, giant eMChA originates from the resonantly enhanced  $\eta$ -odd QM

term;  $((g^{zz})_{\mathbf{k}}^-)^2 \propto G_{\mathbf{k}}^{zz,-}$ . This mechanism works even for  $\eta \lesssim 100\text{K}$ .

Figure 4 **f** depicts the schematic picture of the present eMChA mechanism under the chiral LC state. At a fixed  $T (< T_{\text{LC}})$ , the LC order  $\eta$  is fixed to  $+\eta_0$  or  $-\eta_0$ , and its sign is switched by  $B_z$  because  $M_{\text{orb}}$  is the odd-function of  $\eta$  in the  $3Q$  LC state. This fact leads to the sign reversal of the NLH and eMChA by tiny  $B_z$  below  $\min\{T_{\text{LC}}, T_{\text{st}}\}$ , where  $T_{\text{st}}$  is the stripe CDW transition temperature. This result is consistent with the experimental report of the eMChA in Ref. [29]. We stress that  $\sigma_{zzz,x}$  is proportional to the AB direction order  $\eta_1$ , so the eMChA is induced by the  $1Q$ -LC when its direction is parallel to the stripe CDW. Importantly, in Ref. [46], no eMChA is observed in  $\text{KV}_3\text{Sb}_5$ , in which the  $3Q$ -LC emerges while no stripe CDW is observed experimentally. This observation is naturally explained by the preset scenario.

## SUMMARY

In this paper, we have identified the microscopic mechanism underlying the giant eMChA originating from chiral LC in kagome metals, based on the derived exact formulas for eMChA and NLH with respect to the dominant terms for  $\tau v_F \gg 1$ . Under the chiral LC order  $\eta$ , significant eMChA conductivity ( $\propto \eta \tau^3 I_{\text{st}}$ ) and NLH one ( $\propto \eta \tau^2 I_{\text{st}}$ ) manifest in the presence of  $2a_0$  or  $4a_0$  stripe CDW that is universally observed in  $\text{CsV}_3\text{Sb}_5$ . The eMChA originates from the TRS breaking dipole potential  $\epsilon_{\mathbf{k}}^- \propto k_y \eta I_{\text{st}}$ . Notably, eMChA experiences a dramatic amplification (by  $\sim 100$  times) due to resonantly enhanced QM effects arising from band reconstruction in the LC phase across a broad parameter range. This mechanism leads to substantial eMChA even when the LC order  $\eta$  is small (approximately  $\sim T_{\text{LC}} = 30 \sim 100\text{K}$ ), underscoring the critical role of quantum geometry in kagome metals. Importantly, in Ref. [46], no eMChA is observed in  $\text{KV}_3\text{Sb}_5$ , in which the  $3Q$ -LC emerges while no stripe CDW is observed experimentally. This observation is naturally explained by the preset theory. The present study manifests that kagome metal is an ideal platform for developing quantum geometric effects in strongly correlated metals.

The primary achievements of this study are summarized as follows: (i) Derivation of essential electronic properties and their symmetries in multi-quantum orders of kagome metals through the experimental reports of the eMChA [29]. (ii) Discovery of a novel QM mechanism responsible for giant and field-tunable eMChA, highlighting the importance of quantum geometry in kagome metals. (iii) Development of nonreciprocal transport theory utilizing the QM in strongly correlated metals, like various kagome metals, chiral magnets [42, 43], and loop-

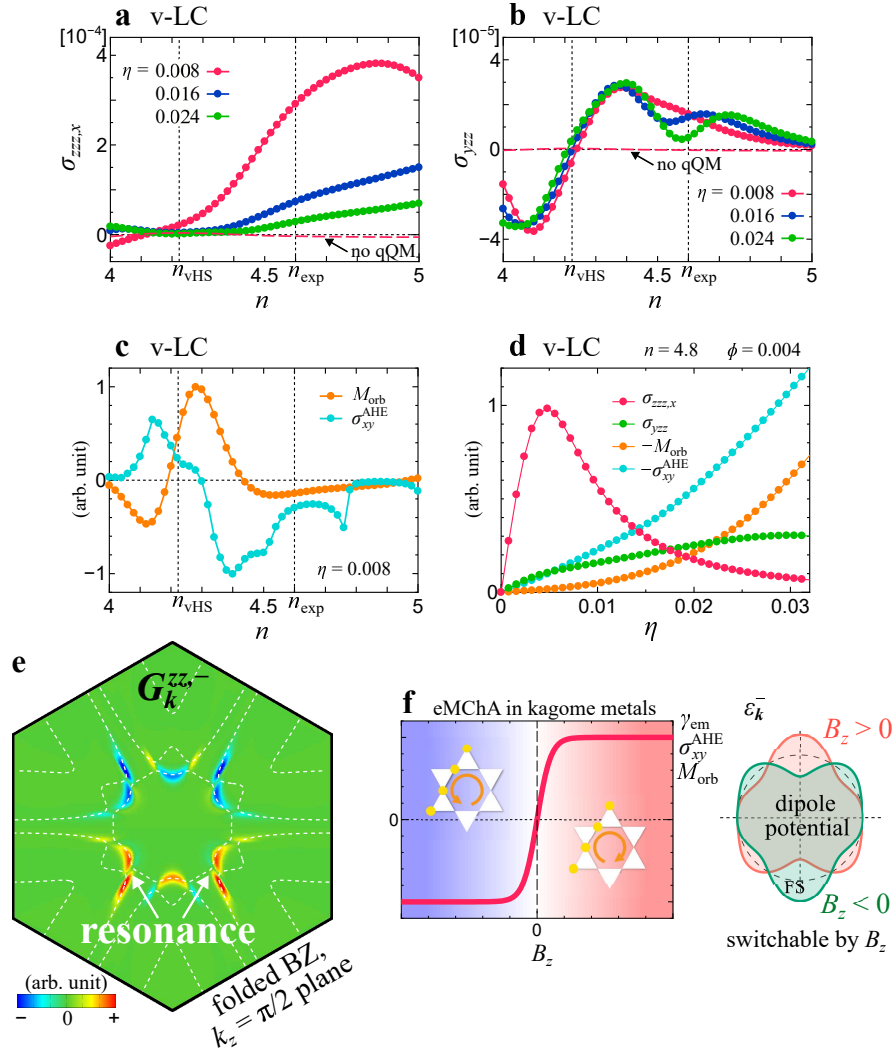


FIG. 4. **Obtained NLH and eMChA conductivities.** **a.** eMChA and **b.** NLH conductivities in the v-LC state with AB direction  $2a_0$  stripe CDW ( $I_{st} = 0.01$ ) as functions of  $n$  for  $\eta = 0.008 - 0.024$ . We put  $\gamma = 1$  for simplicity. The numerical result is almost unchanged for the s-LC state; see Appendix D. **c.**  $M_{\text{orb}}$  and  $\sigma_{xy}^{\text{AHE}}$  as functions of  $n$  in the v-LC state in the arbitrary unit. **d.**  $\eta$ -dependences of the eMChA, NLH,  $M_{\text{orb}}$  and  $\sigma_{xy}^{\text{AHE}}$  as functions of  $\eta$  at  $n = 4.8$ , in the presence of small BO  $\phi = 0.004$ . Only eMChA exhibits a resonance-like enhancement at  $\eta \sim 0.005$ . **e.**  $\eta$ -odd part of the QM at the Fermi level,  $G_{\mathbf{k}}^{zz,-}$  on the  $\mathbf{k}_z = \pi/2$  plane. Its resonant positions are the same as those of  $\sigma_{zzz,x}^-(\mathbf{k})$  in Fig. 3 e. Thus, giant eMChA originates from the resonantly enhanced  $\eta$ -odd QM. **f.** Jump in the eMChA, NLH,  $M_{\text{orb}}$  and AHE as function of  $B_z$  below  $\min\{T_{\text{LC}}, T_{\text{st}}\}$ , where the sign of  $\eta$  is switched by the direction of  $B_z$  while  $|\eta|$  is fixed.

current phase of cuprate superconductors [25].

Here, we briefly discuss several experimental evidence of the LC state. Recent transport measurement of highly symmetric fabricated  $\text{CsV}_3\text{Sb}_5$  micro sample [26] reveals that small magnetic field  $h_z$  ( $< 10\text{T}$ ) or small strain strongly magnifies the LC order in the BO phase. The realized BO+LC coexisting state becomes nematic as shown in Fig. 4 c of Ref. [20] based on the GL free-energy theory. The  $h_z$ -induced enhancement of the LC order is also observed by  $\mu\text{SR}$  measurements [21, 23, 24] and field-tuned chiral transport study [29]. Also, the nematic BO+LC coexisting state has been reported by the STM measurement [79]. In addition, recent magnetic

torque measurements [31] reveal the emergence of the  $1Q$ -LC order above  $T_{\text{BO}}$ , and the  $1Q \rightarrow 3Q$  LC transition occurs under the conical magnetic field. We stress that the eMChA is induced by the  $1Q$ -LC when its direction is parallel to the stripe CDW in the present mechanism. We note that the LC order will have a significant impact on the superconductivity, such as leading to the PDW and the  $4e, 6e$  pairing states [32–34].

We comment on a different kagome metal with double-layer structure  $\text{ScV}_6\text{Sn}_6$ , which exhibits the  $\sqrt{3} \times \sqrt{3}$  CDW [80]. It was proposed that the CDW originates from the flat phonon modes with Sn vibrations [81, 82]. Interestingly,  $\text{ScV}_6\text{Sn}_6$  exhibits the spontaneous TRS

breaking in the CDW phase [83]. The LC-induced QM effects in such different kagome metals would be an interesting future problem.

In this paper, we studied the eMChA and NLH conductivities in the LC phase due to the nonlinear Drude mechanism. When the stripe CDW is along the  $y$ -direction (=AB direction), the  $\eta$ -odd qQM dipole  $g^{zz,-} \propto k_y$  emerges. Then, we obtain  $\sigma_{zzz,x}^- \sim \tau^3 \eta I_{\text{st}}$  and  $\sigma_{zzz,y}^- = 0$ . We also obtain  $\sigma_{yzz}^- \sim \tau^2 \eta I_{\text{st}}$  and  $\sigma_{xzz}^- = 0$ . (Here,  $\eta$ -even eMChA and NLH always vanish.) In addition, the Berry-curvature mechanism has been studied theoretically in Ref. [29]. The  $\eta$ -even Berry curvature dipole  $\Omega^{y,+} \propto k_z$  gives rise to  $\sigma_{zzz,y}^+ \sim \tau^2 \eta^2 I_{\text{st}}$  and  $\sigma_{zzz,x}^+ = 0$ ; see the discussion in Appendix C. The same mechanism gives  $\sigma_{xzz}^+ \sim \tau \eta^2 I_{\text{st}}$  and  $\sigma_{yzz}^+ = 0$  [56]. (In this scenario,  $\eta$ -odd eMChA and NLH always vanish.) Consequently, the eMChA and NLH tensors originating from the nonlinear Drude and Berry curvature mechanisms exhibit distinct symmetries. This distinction is crucial for identifying the microscopic mechanisms governing nonlinear transport phenomena. Both contributions would coexist in kagome metals.

### Acknowledgments

We are grateful to S. Onari, Y. Matsuda, T. Shibauchi, K. Hashimoto, and T. Asaba for fruitful discussions.

### A: GL free energy for kagome metals:

In 2D kagome lattice model, the Ginzburg-Landau (GL) free energy without magnetic field ( $\mathbf{B} = \mathbf{0}$ ) is  $F = F_\eta + F_\phi + F_{\eta,\phi}$  [17, 20], where

$$F_\phi = a_b |\phi|^2 + b_1 \phi_1 \phi_2 \phi_3 + d_1 (\phi_1^4 + \phi_2^4 + \phi_3^4) + d_2 (\phi_1^2 \phi_2^2 + \text{cycl.}), \quad (\text{S1})$$

$$F_\eta = a_c |\eta|^2 + d_3 (\eta_1^4 + \eta_2^4 + \eta_3^4) + d_4 (\eta_1^2 \eta_2^2 + \text{cycl.}) \quad (\text{S2})$$

and  $F_{\eta,\phi}$  contains the current-bond cross terms proportional to  $\eta^2 \phi^1$  and  $\eta^2 \phi^2$ :

$$F_{\eta,\phi} = b_2 (\phi_1 \eta_2 \eta_3 + \text{cycl.}) + 2d_5 (\phi_1^2 \eta_1^2 + \phi_2^2 \eta_2^2 + \phi_3^2 \eta_3^2) + d_6 (\phi_1^2 \eta_2^2 + \text{cycl.}) \quad (\text{S3})$$

Here,  $a_x = r_x (T - T_x^0)$  ( $x = c$  or  $b$ ), where  $T_{c(b)}^0$  is the current-order (BO) transition temperature without other orders. Theoretically,  $a_x \sim N(0)(-1 + \lambda_x^{-1})$ , where  $N(0)$  is the density-of-states ( $\sim 1 \text{ eV}^{-1}$ ) and  $\lambda_x$  is the DW equation eigenvalue of the current order ( $x = c$ ) or the bond order ( $x = b$ ) [69].  $\lambda_x = 1$  at  $T = T_x^0$ , while  $\lambda_x = 0$  (*i.e.*,  $a_x = \infty$ ) in the absence of interaction.

This GL free energy theory can be extended to the 3D kagome metals. Hereafter, we assume the  $2 \times 2 \times 2$  order parameters. First, we consider the case where only the BO parameters are finite. Then, we set  $\phi = (\phi_1, \phi_2, \phi_3)$  for the first layer, and  $\phi' = (e^{i\psi_1} \phi_1, e^{i\psi_2} \phi_2, e^{i\psi_3} \phi_3)$  for the second layer. Here,  $\psi = (\psi_1, \psi_2, \psi_3)$  is the set of the phase shifts. The  $3Q$  BO is stabilized by the 3rd-order  $b_1$ -term, which is finite when  $\psi_1 + \psi_2 + \psi_3 = 0 \pmod{2\pi}$  [25]. By considering the 3rd-order GL free energy, we hereafter study the following two cases: (i)  $\psi = (0, 0, 0)$ , which represents the  $2 \times 2 \times 1$  vertical-stack BO. (ii)  $\psi = (0, \pi, \pi)$ ,  $(\pi, 0, \pi)$ , and  $(\pi, \pi, 0)$ , each of which represents the  $2 \times 2 \times 2$  shift-stack BO.

We also consider the case where only the LC parameters are finite. Then, we set  $\eta = (\eta_1, \eta_2, \eta_3)$  for the first layer, and  $\eta' = (e^{i\theta_1} \eta_1, e^{i\theta_2} \eta_2, e^{i\theta_3} \eta_3)$  for the second layer. Here,  $\theta = (\theta_1, \theta_2, \theta_3)$  is the set of the phase shifts. Note that the 3rd-order term  $b'_1 \eta_1 \eta_2 \eta_3$  is absent in the GL free energy (*i.e.*,  $b'_1 = 0$ ) because it should be TRS invariant. Then, the  $3Q$  LC  $\eta_m = \eta e_m$  ( $m = 0, a \sim c$ ) appears via the 2nd-order phase transition when  $d_4/2d_3 < 1$ . In the opposite case, the  $1Q$  LC appears.

Next, we consider the case where the LC order appears inside the LC phase. Without loss of generality, we set the 3D BO  $\phi = \phi e_0$ , where  $e_0 \equiv (1, 1, 1)/\sqrt{3}$ . This BO is realized when  $b_1 < 0$ . We also introduce  $e_a \equiv (1, -1, -1)/\sqrt{3}$ ,  $e_b \equiv (-1, 1, -1)/\sqrt{3}$ , and  $e_c \equiv (-1, -1, 1)/\sqrt{3}$ . Then, the LC order parameter inside this 3D BO state becomes  $\eta = \eta e_m$  ( $m = a \sim c$ ) and  $\theta = \psi$  to gain the  $b_2$ -term free energy for  $b_2 \sim -b_1 > 0$ . (Here, we have assumed the relation  $|\phi_0| \gg |\eta|$ . The 3D LC order for  $\theta = (0, 0, 0)$  and that for  $\theta = (0, \pi, \pi)$  are respectively shown in Figs. 2 **e** and **g**, respectively. The realized coexisting states exhibits the  $Z_3$  nematic states.

We further introduce the  $2a_0$  stripe along AB axis. When  $(\phi, \eta) = (\phi_0, \eta_m)$ , the relation  $F[\phi_0, \eta_a] \neq F[\phi_0, \eta_{b(c)}]$  is satisfied by the symmetry. Thus, the co-existing state (i)  $m = a$  or (ii)  $m = b$  or  $c$  is realized. (For  $m = a$ ,  $Z_3$  nematicity is parallel to stripe CDW.) In both cases, the free energy is independent of the sign of  $\eta$ .

Next, we introduce the magnetic field  $B_z$ . Then, the field-induced GL free energy is  $\Delta F = -M_{\text{orb}} B_z$ , where the orbital magnetization along the  $z$ -axis is expressed as [25]

$$M_{\text{orb}} = m_1 \phi \cdot \eta + m_2 \eta_1 \eta_2 \eta_3 + m_3 (\eta_1 \phi_2 \phi_3 + \phi_1 \eta_2 \phi_3 + \phi_1 \phi_2 \eta_3). \quad (\text{S4})$$

Thus, the LC order  $\eta$  changes its sign depending on the direction of  $B_z$ . This is important to understand the distinct field-induced change of the eMChA. This result is naturally extended to the  $2 \times 2 \times 2$  LC state. In the case of **a**,  $+\eta_a$  or  $-\eta_a$  is selected depending on the sign of  $m_1 B_z$ , so the LC order  $\eta_a$  is inverted by small  $B_z$ . In the case of **b**, by the same reason, the sign of  $\eta_{b(c)}$  is inverted by small  $B_z$ . Thus, in both cases,  $\sigma_{zzx} \propto \eta_1 (\equiv (\eta)_1)$  is inverted by reversing the sign of  $B_z$ . Therefore, the present theory uncover the reason why LC-induced giant eMChA can be switched by tiny  $B_z$  in kagome metal.

In the case of  $T_{\text{BO}} \gg T_{\text{LC}}$ , the BO is almost fixed as  $\phi_0 = \phi e_0$  for  $b_1 < 0$ . For  $T < T_{\text{LC}}$ , the cLC order is obtained by minimizing the GL free energy as  $\bar{\eta}_m = \eta \bar{e}_m$ , where  $\bar{e}_a = (a, -1, -1)/A$ ,  $\bar{e}_b = (-1, a, -1)/A$ , and  $\bar{e}_c = (-1, -1, a)/A$  with  $A = \sqrt{2 + a^2}$  [25]. Here, we obtain  $a \lesssim 2$  for  $T \lesssim T_{\text{LC}}$  by minimizing the 3rd-order GL free energy, while  $a$  approaches to 1 as the ratio  $|\eta|/|\phi|$  increases due to the 4th-order GL terms [25]. The realized BO+LC order  $(\phi, \eta) = (\phi_0, \bar{\eta}_m)$  ( $m = a \sim c$ ) is the  $Z_3$  nematic state, which is observed experimentally [79]. In the main text, we set  $a = 1$  to simplify the discussion because the essential nature of the eMChA is unchanged.

### B: 3D $d_p + d_m$ orbital kagome lattice model

Here, we introduce the 3D  $d_p + d_m$  orbital kagome lattice model. The intra-layer and inter-layer hopping integrals are shown in Figs. S1 **a** and **b**, respectively. In Fig. S1 **a**, the nearest and the third-nearest  $d_p$ - $d_p$  hopping integrals are  $t_p = -0.5$  and  $t'_p = -0.08$ , respectively. The nearest  $d_m$ - $d_m$  hopping integral is  $t_m = -1$ , and the next-nearest one is  $t'_m = 0$ . The nearest  $d_p$ - $d_m$  hopping integral is  $t_{pm} = +0.05$  or  $-0.05$ , whose sign depends on the direction of the hopping by following the Slater-Koster theory. In addition, we introduce the  $d_m$ -orbital on-site energy  $E_m = +2.3$ .

We also introduce the inter-layer hopping integrals shown in Fig. S1 **b**. According to the first-principles study, the  $d_m$ - $d_m$  inter-layer hopping  $t_{m\perp}$  (between A-A

etc.)  $t'_{m\perp}$  (between A-B etc.) are much larger than other inter-layer hopping integrals. Here, we set  $t_{m\perp} = t'_{m\perp} = 0.02$  to reproduce the  $k_z$ -dependence of the vHS energy of the mix-type band ( $=d_m$ -orbital band) [76, 77].

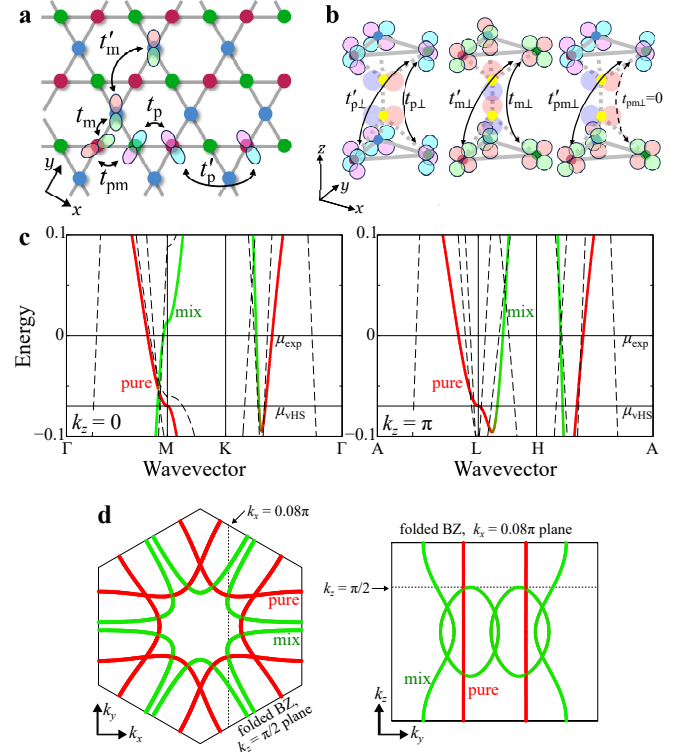


Fig. S1. **3D kagome lattice model parameters.** **a**. Intra-layer hopping integrals and **b**. inter-layer hopping integrals in the present 3D kagome metal model. In the present study, we drop small and unimportant hopping integrals  $t'_m$ ,  $t_{p\perp}$ ,  $t'_{p\perp}$ ,  $t_{pm\perp}$  and  $t'_{pm\perp}$  to simplify the model parameters. **c**. Bandstructure of the present model on the  $k_z = 0$  plane and that on the  $k_z = \pi$  plane. **d**. FSSs in the folded BZ without the LC order ( $\eta = 0$ ). When  $\eta \neq 0$ , the FSSs are changed to those in Fig. 3 **e** in the main text.

At  $n = n_{\text{exp}} (= 4.6)$  the present model reproduces the main  $d$ -orbital FSSs given by the first-principles study very well, as shown in Fig. 3 of the main text. Fig. S1 **c** shows the bandstructures on both  $k_z = 0$  plane and  $k_z = \pi$  plane. The characteristic bandstructure near the Fermi level, such as the vHS saddle-point dispersion around M point, are reproduced qualitatively. Here, the  $d_p$  orbital weight is expressed as red color. Away from the Fermi level, the bandstructure starts to deviate from the DFT one. This deviation gives no serious problem, because only the bandstructure near the Fermi level is important for the eMChA and the NLH conductivities, both of which are the QP transport phenomena ( $\propto \tau^n$  with  $n \geq 1$ ). Fig. S1 **d** gives the FSSs in the folded BZ scheme. By introducing the LC order  $\eta$ , the FSSs are changed to those in Fig. 3 **e** in the main text.

In the main text, we perform the numerical study of

the NLH and eMChA conductivities. The obtained result will be semi-quantitatively reliable for  $n \approx n_{\text{exp}}$ , because the present model well reproduces the FSs given by the first principles study.

### C: Derivations of linear and nonlinear conductivities and $M_{\text{orb}}$

Here, we derive the most divergent non-linear conductivities with respect to the QP lifetime  $\tau$ , which give the most significant contributions in good metals. Here,  $\gamma = 1/2\tau$  is the QP damping rate given as  $-\text{Im}\Sigma^R$ . In this section, we derive the NLH and eMChA conductivities based on the Boltzmann equation method.

For this purpose, we introduce the orbital magnetic moment  $\mathbf{m}_{n,\mathbf{k}}$ , the Berry curvature  $\mathbf{\Omega}_{n,\mathbf{k}}$  of the  $n$ th band. They are given as

$$\begin{aligned} m_{n,\mathbf{k}}^\mu &= \frac{i}{2} \left[ \left\langle \nabla_{\mathbf{k}} u_{n,\mathbf{k}} \left| \times \left( \epsilon_{n,\mathbf{k}} - \hat{h}(\mathbf{k}) \right) \right| \nabla_{\mathbf{k}} u_{n,\mathbf{k}} \right\rangle_\mu \right] \\ &= \frac{1}{2} \sum_{l \neq n} \frac{\epsilon_{\mu\alpha\beta} \text{Im}[v_{n,l}^\alpha v_{l,n}^\beta] \epsilon_{nl,\mathbf{k}}}{(\epsilon_{nl,\mathbf{k}})^2 + \delta^2} \end{aligned} \quad (\text{S5})$$

and

$$\begin{aligned} \Omega_{n,\mathbf{k}}^\mu &= i \left[ \left\langle \nabla_{\mathbf{k}} u_{n,\mathbf{k}} \left| \times \left| \nabla_{\mathbf{k}} u_{n,\mathbf{k}} \right. \right. \right\rangle_\mu \right] \\ &= \sum_{l \neq n} \frac{\epsilon_{\mu\alpha\beta} \text{Im}[v_{n,l}^\alpha v_{l,n}^\beta]}{(\epsilon_{nl,\mathbf{k}})^2 + \delta^2}, \end{aligned} \quad (\text{S6})$$

where  $\epsilon_{nl,\mathbf{k}} \equiv \epsilon_{n,\mathbf{k}} - \epsilon_{l,\mathbf{k}}$  and  $\mu, \alpha, \beta = x, y, z$ . Here, a small constant  $\delta$  is introduced to obtain reliable numerical results, as we did for the QM and qQM in the main text. In deriving Eqs. (S5) and (S6), we have used the relation

$$\langle u_{l,\mathbf{k}} \partial_\mu | u_{m,\mathbf{k}} \rangle = \frac{v_{l,m}^\mu}{\epsilon_{l,\mathbf{k}} - \epsilon_{m,\mathbf{k}}} \quad (\text{S7})$$

and  $v_{l,m}^\mu = \langle u_{l,\mathbf{k}} \partial^\mu \hat{h}(\mathbf{k}) | u_{m,\mathbf{k}} \rangle$  is the matrix element of the velocity operator for the wave vector  $\mathbf{k}$  in the band representation.

Using both  $\Omega^z$  and  $m^z$ , the orbital magnetization  $M_{\text{orb}}$  along the  $z$  axis is give as [84, 85]

$$M_{\text{orb}} = \frac{1}{\pi N} \sum_{n,\mathbf{k}} \left[ m_{n,\mathbf{k}}^z f_{n,\mathbf{k}} - \Omega_{n,\mathbf{k}}^z T \ln \left( 1 + e^{-(\epsilon_{n,\mathbf{k}} - \mu)/T} \right) \right] \quad (\text{S8})$$

Also, the anomalous Hall conductivity at  $T = 0$  is given as [86]

$$\sigma_{xy}^{\text{AHE}} = \sigma_{xy}^{\text{I}} + \sigma_{xy}^{\text{IIa}} + \sigma_{xy}^{\text{IIb}}. \quad (\text{S9})$$

Here,  $\sigma_{xy}^{\text{I}}$ ,  $\sigma_{xy}^{\text{IIa}}$ , and  $\sigma_{xy}^{\text{IIb}}$  are given by

$$\sigma_{xy}^{\text{I}} = -\frac{1}{\pi N} \sum_{l \neq m, \mathbf{k}} \text{Im} \left[ v_{m,l,\mathbf{k}}^x v_{l,m,\mathbf{k}}^y \right] \text{Im} \left[ \frac{1}{\bar{\epsilon}_{l,\mathbf{k}} \cdot \bar{\epsilon}_{m,\mathbf{k}}} \right], \quad (\text{S10})$$

$$\sigma_{xy}^{\text{IIa}} = -\frac{1}{\pi N} \sum_{l \neq m, \mathbf{k}} \frac{\text{Im} \left[ v_{m,l,\mathbf{k}}^x v_{l,m,\mathbf{k}}^y \right]}{\epsilon_{l,\mathbf{k}} - \epsilon_{m,\mathbf{k}}} \text{Im} \left[ \frac{\bar{\epsilon}_{l,\mathbf{k}} + \bar{\epsilon}_{m,\mathbf{k}}}{\bar{\epsilon}_{l,\mathbf{k}} \cdot \bar{\epsilon}_{m,\mathbf{k}}} \right], \quad (\text{S11})$$

and

$$\sigma_{xy}^{\text{IIb}} = \frac{2}{\pi N} \sum_{l \neq m, \mathbf{k}} \frac{\text{Im} \left[ v_{m,l,\mathbf{k}}^x v_{l,m,\mathbf{k}}^y \right]}{(\epsilon_{l,\mathbf{k}} - \epsilon_{m,\mathbf{k}})^2} \text{Im} \left[ \ln \left( \frac{\bar{\epsilon}_{l,\mathbf{k}}}{\bar{\epsilon}_{m,\mathbf{k}}} \right) \right], \quad (\text{S12})$$

respectively. Here,  $\bar{\epsilon}_{l,\mathbf{k}} \equiv \epsilon_{l,\mathbf{k}} - \mu - i\gamma$ , and  $\gamma (> 0)$  is the imaginary part of the self-energy.  $\sigma_{xy}^{\text{I}}$  and  $\sigma_{xy}^{\text{IIa}}$  are the contribution from the FS while  $\sigma_{xy}^{\text{IIb}}$  is the contribution from the Fermi sea by the Berry curvature:  $\sigma_{xy}^{\text{IIb}} \propto \sum_{n,\mathbf{k}} \Omega_{n,\mathbf{k}} f_{n,\mathbf{k}}$  for  $\gamma \rightarrow 0$  at  $T \rightarrow 0$ . We note that  $\sigma_{xy}^{\text{AHE}}$  also vanishes when the global TRS is preserved.

Next, we introduce the quasi-classical kinetic equations of the wave-packet [87]

$$\dot{\mathbf{r}} = \nabla_{\mathbf{k}} \tilde{\epsilon}_{\mathbf{k}} - \dot{\mathbf{k}} \times \mathbf{\Omega}_{\mathbf{k}}, \quad (\text{S13})$$

$$\dot{\mathbf{k}} = -\mathbf{E} - \dot{\mathbf{r}} \times \mathbf{B}, \quad (\text{S14})$$

where  $\tilde{\epsilon}_{\mathbf{k}} \equiv \epsilon_{\mathbf{k}} - \mathbf{m}_{\mathbf{k}} \cdot \mathbf{B}$ . These coupled equations with respect to  $\dot{\mathbf{r}}$  and  $\dot{\mathbf{k}}$  are solved as

$$D_{\mathbf{k}} \dot{\mathbf{r}} = \nabla_{\mathbf{k}} \tilde{\epsilon}_{\mathbf{k}} + \mathbf{E} \times \mathbf{\Omega}_{\mathbf{k}} + (\nabla_{\mathbf{k}} \tilde{\epsilon}_{\mathbf{k}} \cdot \mathbf{\Omega}_{\mathbf{k}}) \mathbf{B}, \quad (\text{S15})$$

$$D_{\mathbf{k}} \dot{\mathbf{k}} = -\mathbf{E} - \nabla_{\mathbf{k}} \tilde{\epsilon}_{\mathbf{k}} \times \mathbf{B} - (\mathbf{E} \cdot \mathbf{B}) \mathbf{\Omega}_{\mathbf{k}}, \quad (\text{S16})$$

where  $D_{\mathbf{k}} = 1 + \mathbf{B} \cdot \mathbf{\Omega}_{\mathbf{k}}$  [87]. Then, the macroscopic current is given as

$$\mathbf{j} = -\frac{1}{N} g_s \sum_{\mathbf{k}} D_{\mathbf{k}} \dot{\mathbf{r}} f, \quad (\text{S17})$$

$$\dot{\mathbf{k}} \cdot \nabla_{\mathbf{k}} f = \frac{f_0 - f}{\tau} \quad (\text{S18})$$

where  $f_0$  is the Fermi distribution function for  $\epsilon_{\mathbf{k}}$ . In the relaxation time approximation, the collision integral is expressed as  $\frac{f_0 - f}{\tau}$  in Eq. (S18), where  $\tau$  is the relaxation time of the wave-packet. Then, we can expand the distribution function as  $f = \sum_{n=0}^{\infty} f_n$ , where  $f_n \propto \tau^n$ . Then, Eq. (S18) is expressed as

$$\sum_{n=0}^{\infty} \dot{\mathbf{k}} \cdot \nabla_{\mathbf{k}} f_n = -\frac{1}{\tau} \sum_{n=1}^{\infty} f_n, \quad (\text{S19})$$

Thus, we obtain the recurrence formula  $f_{n+1} = -\tau B f_n$ , where  $B = \frac{1}{D_{\mathbf{k}}} (-\mathbf{E} - \nabla_{\mathbf{k}} \tilde{\epsilon}_{\mathbf{k}} \times \mathbf{B} - (\mathbf{E} \cdot \mathbf{B}) \mathbf{\Omega}_{\mathbf{k}}) \cdot \nabla_{\mathbf{k}}$ . Using the derived  $f_n$ , we can derive the linear and non-linear conductivities based on Eq. (S17).

First, we derive the linear conductivities in metals, by focusing the most divergent term with respect to  $\tau = 1/2\gamma$  [53]. The longitudinal conductivity along the  $\mu$ -axis

is given by the  $E^1 B^0$  term of  $f_1$ , where we are allowed to set  $\mathbf{\Omega}_{\mathbf{k}} = \mathbf{m}_{\mathbf{k}} = \mathbf{0}$ :

$$\sigma_{\mu\mu} = -e^2 \frac{g_s}{N} \sum_{a,\mathbf{k}} f'_a(v^\mu v^\mu)_{a,\mathbf{k}} \frac{1}{2\gamma}, \quad (\text{S20})$$

where  $a$  is the band index. The Hall conductivity  $\sigma_{\mu\nu}$  under the magnetic field  $B_\alpha$  is given by the  $E^1 B^1$  term of  $f_2$ :

$$\sigma_{\mu\nu}^{\text{norm},\alpha} = B_\alpha e^3 \frac{g_s}{N} \sum_{a,\mathbf{k}} f'_a(v^\mu d^{\alpha,\nu})_{a,\mathbf{k}} \frac{1}{4\gamma^2}, \quad (\text{S21})$$

where  $d^{\alpha,\nu} \equiv \epsilon_{\alpha\beta\delta} v^\beta v^{\delta\nu}$ , and we set  $B_\alpha = 1$  at the end. Note that  $\sigma_{\mu\nu}^{\text{norm},\alpha}$  is finite when  $\mu \neq \nu \neq \alpha$ . Then, the Hall coefficient in the  $\mu\nu$ -plane is given by  $R_H = \sigma_{\mu\nu}^{\text{norm},\alpha} / \sigma_{\mu\mu} \sigma_{\nu\nu}$ . Finally, the magnetoconductivity  $\Delta\sigma_{\mu\mu}^\alpha$  under the magnetic field  $B_\alpha$  is given by the  $E^1 B^2$  term of  $f_3$ :

$$\Delta\sigma_{\mu\mu}^\alpha = -B_\alpha^2 e^4 \frac{g_s}{N} \sum_{a,\mathbf{k}} f'_a(\{d^{\alpha,\mu}\}^2)_{a,\mathbf{k}} \frac{1}{8\gamma^3}, \quad (\text{S22})$$

which is always negative, and we set  $B_\alpha = 1$  at the end. Then, the magnetoresistance (MR) under the magnetic field along the  $\alpha$ -axis up to  $O(B_\alpha^2)$  is given by  $\rho_{\mu\mu}(B_\alpha) = \rho_{\mu\mu}(0) + [-\Delta\sigma_{\mu\mu}^\alpha / \sigma_{\mu\mu} - (\sigma_{\mu\nu}^{\text{norm},\alpha})^2 / \sigma_{\mu\mu} \sigma_{\nu\nu}] B_\alpha^2$ , where  $\nu \neq \mu \neq \alpha$ .

Here, we consider the MR along the  $z$  axis  $\rho_{zz}(B_x)$ , which is  $\eta$ -even. According to Eq. (S22),  $\Delta\sigma_{zz}^\alpha \propto \sum_{a,\mathbf{k}} f'_a(\{d^{x,z}\}^2)_{a,\mathbf{k}} \gamma^{-3}$  and  $d^{x,z} = v^y v^{zz} - v^z v^{yz}$ . The  $(v^{\mu\nu})^2$ -term enhances the  $\rho_{zz}$  in the  $2 \times 2$  LC state, due to the qQM term in  $v^{\mu\nu}$ . We present the numerical analysis in Appendix E.

Next, we derive the most divergent nonlinear conductivities in noncentrosymmetric metals with respect to  $\tau = 1/2\gamma$ . The NLH and eMChA conductivities are given by the  $E^2 B^0$  term in  $f_2 \propto \tau^2$  and the  $E^2 B^1$  terms in  $f_3 \propto \tau^3$ , respectively. They are derived from  $f_i$  by setting  $\mathbf{\Omega}_{\mathbf{k}} = \mathbf{m}_{\mathbf{k}} = \mathbf{0}$ . These most-divergent terms are finite when both IS and TRS are broken. Here, we derive only  $\sigma_{yzz}$  and  $\sigma_{zzz,x}$  for simplicity. Their expressions are obtained as

$$\begin{aligned} \sigma_{\alpha\beta\beta} &= -e^3 \frac{g_s}{N} \sum_{a,\mathbf{k}} (\varphi^\alpha \partial_\beta \partial_\beta f)_{a,\mathbf{k}} \frac{1}{4\gamma^2}, \\ &= e^3 \frac{g_s}{N} \sum_{a,\mathbf{k}} f'_a(v^{\alpha\beta} v^\beta)_{a,\mathbf{k}} \frac{1}{4\gamma^2}, \end{aligned} \quad (\text{S23})$$

$$\begin{aligned} \sigma_{\alpha\beta\beta,\gamma} &= e^4 g_s \sum_{a,\mathbf{k}} \epsilon^{\gamma\phi\eta} (v^\alpha (v^\phi \partial_\eta) \partial_\beta \partial_\beta f \\ &\quad + v^\alpha \partial_\beta (v^\phi \partial_\eta) \partial_\beta f)_{a,\mathbf{k}} \tau^3 \\ &= e^4 g_s \sum_{a,\mathbf{k}} \epsilon^{\gamma\phi\eta} (2v^{\alpha\beta\eta} v^\phi v^\beta f' \\ &\quad + v^{\alpha\eta} v^\beta \phi v^\beta f')_{a,\mathbf{k}} \tau^3, \end{aligned} \quad (\text{S24})$$

which are canceled the nonlinear Drude mechanism, and we set  $B_\alpha = 1$  in Eq. (S24). (The relations  $\epsilon^{\gamma\phi\eta} v^\phi v^\eta = \epsilon^{\gamma\phi\eta} v^\phi v^\eta = 0$  are used in the derivation.) These nonlinear conductivities are odd-functions of the LC order  $\eta$ . The expression of  $\sigma_{\alpha\beta\beta,\gamma}$  in the main text is given by the partial integral of the first term in the last line of Eq. (S24) with respect to  $k_\eta$ . The second term in the last line of Eq. (S24) vanishes when  $\alpha = \beta$ .

In the presence of the TRS, the nonlinear Drude terms in Eqs. (S23) and (S24) vanish. In this case, the most divergent NLH and eMChA conductivities are given by the  $E^2 B^0$  term in  $f_1 \propto \tau^1$  and the  $E^2 B^1$  terms in  $f_2 \propto \tau^2$ , respectively. They are expressed as the summation of the  $\mathbf{\Omega}_{\mathbf{k}}$ -linear and the  $\mathbf{m}_{\mathbf{k}}$ -linear terms. Here, we derive only  $\sigma_{\mu zz}$  and  $\sigma_{zzz,\mu}$  ( $\mu = x, y$ ) for simplicity. Their expressions are obtained as

$$\sigma_{\mu zz} = -e^2 \frac{g_s}{N} \sum_{a,\mathbf{k}} \epsilon_{\mu\delta z} f'_a(v^z \Omega^\delta)_{a,\mathbf{k}} \frac{1}{2\gamma}, \quad (\text{S25})$$

$$\begin{aligned} \sigma_{zzz,\mu} &= -B_y e^3 \frac{g_s}{N} \sum_{a,\mathbf{k}} f'_a(v^{zz} \partial_z m^\mu + v^z \partial_{zz} m^\mu)_{a,\mathbf{k}} \frac{1}{4\gamma^2}, \\ &\quad - B_y e^3 \frac{g_s}{N} \sum_{a,\mathbf{k}} f'_a(2v^{zz} v^z \Omega^\mu + (v^z)^2 \partial_z \Omega^\mu)_{a,\mathbf{k}} \frac{1}{4\gamma^2}, \end{aligned} \quad (\text{S26})$$

where we set  $B_\alpha = 1$  in Eq. (S26). Here, we introduce  $\Omega^{\mu,\pm} = [\Omega^\mu(\eta) \pm \Omega^\mu(-\eta)]/2$ . Figure S2 shows the obtained  $\mathbf{a} \Omega_{a,\mathbf{k}}^{y,+}$  and  $\mathbf{b} \Omega_{a,\mathbf{k}}^{y,-}$  in the LC+stripe CDW state on the  $k_x = 0.14\pi$  plane. It is found that  $\Omega_{a,\mathbf{k}}^{y,+} \sim k_z$  and  $\Omega_{a,\mathbf{k}}^{y,-} \sim k_y k_z$ . The symmetry properties of  $\Omega_{a,\mathbf{k}}^{\mu,\pm}$  are summarized in Table I of the main text. The symmetry of  $m_{a,\mathbf{k}}^{\mu,\pm}$  is the same as that of  $\Omega_{a,\mathbf{k}}^{\mu,\pm}$ . Thus, the dipole components  $\Omega_{a,\mathbf{k}}^{y,+}, m_{a,\mathbf{k}}^{y,+} \sim k_z$  give rise to the NLH  $\sigma_{xzz}$  and eMChA  $\sigma_{zzz,y}$ . However, neither  $\Omega_{a,\mathbf{k}}^{y,-}$  nor  $m_{a,\mathbf{k}}^{y,-}$  contribute to the eMChA and the NLH. Therefore, Eqs. (S25) and (S26) are NOT switchable by the direction of  $B_z$ . In addition, Eq. (S24) would dominate over Eq. (S26) in good metals with  $\tau v_F \gg 1$ . For these reasons, we study the nonlinear Drude mechanism given in Eqs. (S23) and (S24) in the present paper.

#### D: Numerical study of NLH and eMChA in LC+B0 states

In Fig. 4 of the main text, we calculated the NLH and eMChA due to the v-LC order and the stripe CDW. Here, we perform the same analysis for the s-LC state. Fig. S3 **a** and **b** show the obtained  $\sigma_{zzz,x}$  and  $\sigma_{yzz}$  for the s-LC state, where  $\phi = \phi e_0$ ,  $\eta = \eta e_a$ , and  $\psi = \theta = (0, \pi, \pi)$  under the AB direction stripe CDW. Here, we set  $\eta = 0.008 \sim 0.024$  and  $I_{\text{st}} = 0.01$ . The obtained results are very similar to those for the v-LC state shown in Figs.

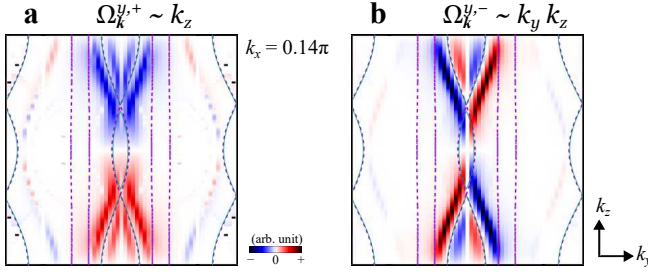


Fig. S2. **Berry curvature of 3D kagome lattice model with LC order + stripe CDW.** Obtained **a.**  $\Omega_k^{y,+}$  and **b.**  $\Omega_k^{y,-}$  in the LC+stripe CDW state on the  $k_x = 0.14\pi$  plane. It is found that  $\Omega_k^{y,+} \sim k_z$  and  $\Omega_k^{y,-} \sim k_y k_z$ . The dipole component  $\Omega_k^{y,+} \sim k_z$  gives rise to the NLH and eMChA, while their signs are unchanged by  $\eta \rightarrow -\eta$ .

4 **a** and **b** in the main text. Therefore, the inter-plane stacking is not essential for both eMChA and NLH.

In Fig. 4 **a** of the main text, we show the eMChA in the v-LC state for  $\eta = 0.008 \sim 0.024$ , where the eMChA takes huge value due to the resonantly magnified QM. In Fig. S3 **c**, we show the eMChA for larger  $\eta$  (0.024, 0.032 and 0.064) at  $I_{st} = 0.01$  as functions of  $n$ . In this region, the eMChA monotonically decreases with  $\eta$  and approaches to the non-resonant value without qQM in  $v^{\mu\nu}$ . Considering that  $T_{LC}$  reported in kagome metals is  $35 \sim 100K$ , the magnitude of the order parameter at  $T = 0$  will be  $|\eta_0| = 0.005 \sim 0.015$  in the case of  $|\eta_0|/T_{LC} \sim 2$ . Therefore, giant eMChA observed in kagome metals is given by the resonantly magnified QM term, which is shown in Fig. 4 **a** of the main text.

We also study the effect of the 3Q BO on the eMChA, which becomes large inside the star-of-David BO state in kagome metals. Fig. S3 **d** shows  $\sigma_{zzz,x}$  obtained for the v-LC state ( $\boldsymbol{\eta} = \eta \mathbf{e}_a$  and  $\boldsymbol{\psi} = (0, 0, 0)$ ) and the v-BO state ( $\phi = \phi \mathbf{e}_0$  and  $\boldsymbol{\theta} = (0, 0, 0)$ ). This LC+BO order led to the  $Z_3$  nematic state whose director is along the AB direction. Here, we set  $\eta = 0 \sim 0.024$ ,  $I_{st} = 0.01$ , and  $\phi = 0.004 \sim 0.008$ . It is found that  $\sigma_{zzz,x}$  is suppressed by  $\phi$ , while it is still large even for  $\phi = 0.008$ .

In Fig. S3 **e**, we show the longitudinal linear conductivities  $\sigma_{xx}$  and  $\sigma_{zz}$  as functions of  $n$  for  $\gamma = 1$ . Here, we set  $\eta = 0.008$  and  $\phi = 0$ , while the obtained results are nearly constant for  $\eta, \phi \lesssim 0.01$ . Both  $\sigma_{xx}$  and  $\sigma_{zz}$  are nearly  $n$ -independent. These results lead to  $\rho_{zz} = 40000\gamma$  [ $\mu\Omega\text{cm}$ ] and  $\rho_{xx} = 2500\gamma$  [ $\mu\Omega\text{cm}$ ]; see the discussion about the experimental units in Appendix E.

Fig. S3 **f** exhibits  $\gamma_{eM} = -\sigma_{zzz,x}/(\sigma_{zz})^2$  for  $I_{st} = 0.01$  and 0.02. Thus,  $\gamma_{eM}$  increases in proportion to  $I_{st}$  at  $n \approx n_{exp}$ .

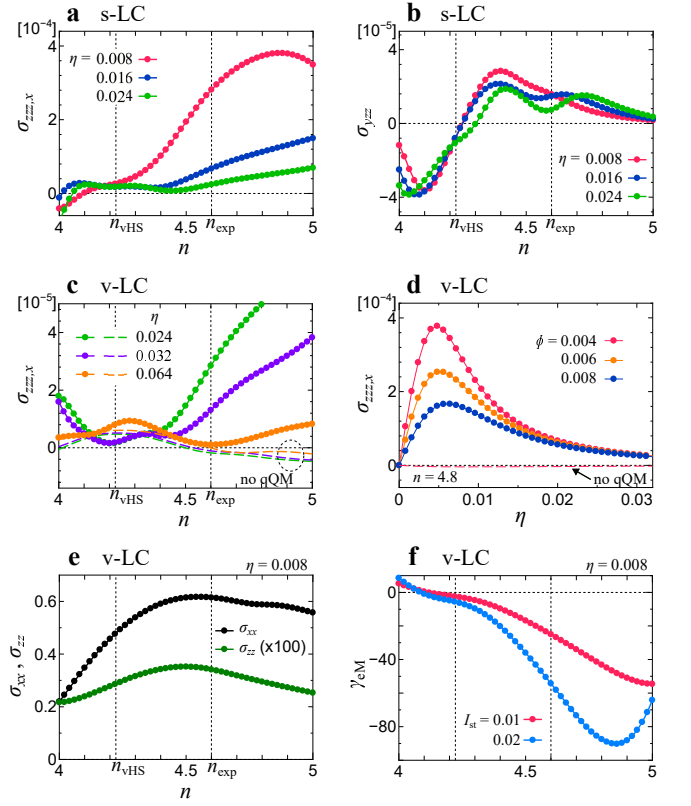


Fig. S3. **NLH and eMChA conductivities in LC + BO state.** **a.** eMChA and **b.** NLH conductivities in the s-LC state with AB direction  $2a_0$  stripe CDW ( $I_{st} = 0.01$ ) as functions of the filling  $n$ . The obtained results are very similar to those for the v-LC state shown in Fig. 4 in the main text. We put  $\gamma = 1$  for simplicity. **c.** eMChA in the v-LC state with  $I_{st} = 0.01$  for larger  $\eta$  (0.024, 0.032 and 0.064) as functions of  $n$ . In this region, the eMChA monotonically decreases with  $\eta$  and approaches to the non-resonant value without qQM in  $v^{\mu\nu}$ . **d.** eMChA  $\sigma_{zzz,x}$  as function of  $\eta$  in the presence of the OB at  $\phi = 0.004$  and 0.008.  $\sigma_{zzz,x}$  is still large even for  $\phi = 0.008$ . **e.**  $\sigma_{xx}$  and  $\sigma_{zz}$  as functions of  $n$  for  $\eta = 0.008$ . Here, we set  $\gamma = 1$ . **f.**  $\gamma_{eM} = -\sigma_{zzz,x}/(\sigma_{zz})^2$  for  $I_{st} = 0.01$  and 0.02. Here, we set  $\gamma = 1$ .

### E: Experimental units of $\sigma_{xxx,z}$ and $\gamma_{eM}$

In the main text, we performed the numerical study in the following units:  $\hbar = e = 1$ , the unit of energy eV, the intra-layer nearest-neighbor distance  $b_0 \equiv |\mathbf{a}_{AB}| = 1$ , and the inter-layer distance  $c_0 = 1$ . In kagome metals,  $b_0 \approx 0.3\text{nm}$  and  $c_0 \approx 1\text{nm}$ . Here, we restore the units of the conductivities in the 3D kagome lattice model with 3-site unit cell, where the volume of the unit cell is  $v_{uc} = 2\sqrt{3}b_0^2c_0$ . (In the 24-site unit cell model with the  $2 \times 2 \times 2$  LC order, the unit cell volume becomes  $8v_{uc}$ . Thus, the derived conductivities should be divided by 8 to obtain the values of the original 3-site unit cell model.)

First, we consider the expression of  $\sigma_{zz}$  given in Eq. (S20) in Appendix. To restore  $\hbar$ ,  $b_0$  and  $c_0$ , we magnify

$\gamma$ ,  $N$ ,  $v^{x(y)}$ , and  $v^z$  with  $\hbar^{-1}$ ,  $v_{uc}$ ,  $b_0\hbar^{-1}$ , and  $c_0\hbar^{-1}$ , respectively. Then, we obtain  $\sigma_{zz}^{\text{exp}} = \left(\frac{e^2}{\hbar}\right) \left(\frac{c_0}{2\sqrt{3}b_0^2}\right) \sigma_{zz}$ , where  $\sigma_{zz} \propto 1/(\gamma \text{ [eV]})$  is the numerical result given in Eq. (S20). Here,  $\hbar/e^2 = 0.42 \times 10^4 \text{ [\Omega]}$  and  $2\sqrt{3}b_0^2/c_0 = 3.1 \times 10^{-10} \text{ [m]}$ . Thus, we obtain  $\rho_{zz} = 40000\gamma \text{ [\mu\Omega cm]}$  because  $\sigma_{zz} \approx 0.0038/(\gamma \text{ [eV]})$  in the Fig. S3 e. In the same way,  $\rho_{xx} = 2500\gamma \text{ [\mu\Omega cm]}$  because  $\sigma_{xx} \approx 0.6/(\gamma \text{ [eV]})$  in the Fig. S3 e. Therefore, we obtain  $\rho_{zz} = 40 \text{ [\mu\Omega cm]}$  and  $\rho_{xx} = 2.5 \text{ [\mu\Omega cm]}$  for  $\gamma = 10^{-3} \text{ [eV]}$ . Experimentally,  $\rho_{zz}^{\text{exp}} \approx 30 \text{ [\mu\Omega cm]}$  at  $\mathbf{B} = 0$  [29], and  $\rho_{xx} = 0.4 \text{ [\mu\Omega cm]}$  in high-quality samples [11]. Therefore,  $\gamma \lesssim 10^{-3} \text{ [eV]}$  is expected to be realized at  $T \approx 0$ . The observed giant MR  $\Delta\rho_{zz}(|\mathbf{B}|)$  indicates that the quantum limit  $\omega_H\tau \gg 1$  is satisfied for  $|\mathbf{B}| \gtrsim 5 \text{ T}$  [29].

Now, we consider  $\gamma_{\text{eM}} = -\sigma_{zzz,x}(\rho_{zz})^2$ , by which the nonlinear resistance is expressed as  $\frac{\rho_{zz}}{\rho_{zz}^0}(1 + \gamma_{\text{eM}}B_xJ_z)$ . (Exactly speaking,  $\gamma_{\text{eM}}^{abc,d} = -\rho_{aa'}(\sigma_{a'bb',d})\rho_{b'c}$ , which gives the nonlinear resistance  $\rho_{ae}(\mathbf{B}, \mathbf{j}) = (\delta_{ab} + \gamma_{\text{eM}}^{abc,d}j_cB_d)\rho_{bc}$ . Note that  $\rho_{ac}\sigma_{cb} = \delta_{ab}$  [88].) Based on the expression of  $\sigma_{zzz,x}$  given in Eq. (S24) in Appendix, we can restore  $\hbar$ ,  $b_0$  and  $c_0$  as explained above. (Note that  $v^{zz}$  and  $v^{yz}$  are multiplied with  $c_0^2/\hbar$  and  $b_0c_0/\hbar$ , respectively.) Then, we obtain  $\sigma_{zzz,x}^{\text{exp}} = \left(\frac{e^2}{\hbar}\right)^2 \left(\frac{c_0^3}{2\sqrt{3}b_0^3}\right) \mu_B \left(\frac{\hbar}{e}\right) \left(\frac{2}{E_{b_0}}\right) \sigma_{zzz,x}$ , where  $\mu_B = e\hbar/2m_e = 5.8 \times 10^{-5} \text{ [eVT}^{-1}]$  is Bohr magneton, where  $m_e$  is the bare electron mass.  $e^2/\hbar = 2.4 \times 10^{-4}[\Omega^{-1}]$  and  $\hbar/e = 3.5 \times 10^3 \text{ [eVA}^{-1}]$ .  $E_{b_0} \equiv \hbar^2/m_e b_0^2$  is 0.89 [eV] for  $b_0 = 0.3\text{nm}$ . (Note that  $E_{b_0} = m_e c^2 \times 10^{-6} = 0.51 \text{ [eV]}$  when  $b_0 = 1000\lambda_e = 3.9 \times 10^{-10} \text{ [m]}$ , where  $\lambda_e = \hbar/m_e c$ ; see Ref. [25].) The numerical study in Fig. 4 a gives  $\sigma_{zzz,x} = S_{\text{eM}}/(\gamma \text{ [eV]})^3$ , where  $S_{\text{eM}} \sim 2 \times 10^{-4}$  for  $\eta \sim 0.008$  and  $I_{\text{st}} \sim 0.01$  at  $n \sim n_{\text{exp}}$ . (The obtained  $\sigma_{zzz,x}$  would not be affected by the  $p$ -orbital bands, which are dropped in the present model, considering the smallness of the  $p$ - $d$  hybridization.) Then, we obtain  $\gamma_{\text{eM}}^{\text{exp}} \sim 10^{-21}/(\gamma \text{ [eV]})^3 \text{ [A}^{-1}\text{T}^{-1}\text{m}^2]$  if the experimental resistivity  $\rho_{zz}(B_x) \sim 500 \text{ [\mu\Omega cm]}$  for  $B_x = 18 \text{ T}$  is applied. When  $\gamma \sim 0.5 \times 10^{-3} \text{ [eV]}$ , the obtained  $\gamma_{\text{eM}}^{\text{exp}}$  reaches  $\sim 10^{-11} \text{ [A}^{-1}\text{T}^{-1}\text{m}^2]$ .

In Ref. [29], giant  $\gamma_{\text{eM}} \sim 10^{-11} \text{ [A}^{-1}\text{T}^{-1}\text{m}^2]$  is reported in  $\text{CsV}_3\text{Sb}_5$  by taking the difference between  $B_x = 18 \text{ T}$  and  $-18 \text{ T}$ . Although  $\rho_{zz}(B_x) \approx 30 \text{ [\mu\Omega cm]}$  at  $B_x = 0$ .  $\rho_{zz}$  is drastically enlarged due to its large MR:  $z \equiv \frac{\rho_{zz}(18\text{T})}{\rho_{zz}(0)} \approx 20$  at  $T = 5\text{K}$ . The observed large MR does not saturate in the quantum limit  $\omega_H\tau \gg 1$  ( $\omega_H \equiv e|\mathbf{B}|/m_Hc$ ) due to the open-orbit FS along the  $k_z$  axis.

We also study the expression  $\gamma_{\text{eM}} = -[\text{Eq.}(S26)]/[\text{Eq.}(S20)]^2$  for  $\mu = z$ . Its experimental units are restored as  $\gamma_{\text{eM}}^{\text{exp}} \approx -\mu_B \left(\frac{\hbar}{e}\right) \frac{4\sqrt{3}b_0c_0}{E_{b_0}} \gamma_{\text{eM}} \approx$

$-\frac{0.5 \times 10^{-18}}{E_{b_0}} \gamma_{\text{eM}} \text{ [A}^{-1}\text{T}^{-1}\text{m}^2]$ , where  $\gamma_{\text{eM}}$  is the present numerical result in unit  $\text{eV}^{-1}$ . Because  $|\gamma_{\text{eM}}| \sim 20/(\gamma \text{ [eV]})$  in the Fig. S3 f, we obtain  $|\gamma_{\text{eM}}^{\text{exp}}| \sim 10^{-14} \text{ [A}^{-1}\text{T}^{-1}\text{m}^2]$  for  $\gamma \sim 10^{-3}$ . It is magnified by the factor  $z^2 \gtrsim 10^2$  by taking account of the magnetoresistance. Thus, the present theory can explain giant  $\gamma_{\text{eM}}$  in kagome metals by considering the giant enhancement factor  $z^2$ .

To summarize, the giant eMChA in kagome metal is given by the ‘‘QM mechanism’’ in the LC phase. The present eMChA is drastically magnified by the ‘‘pure-mix resonance’’ due to the band-folding in the  $2 \times 2$  LC phase. In fact, the eMChA is proportional to  $\sum_{\mathbf{k}} v^{y,+}((g^{zz})^2 - f'_0) \propto \sum_{\mathbf{k}} v^{y,+} G^{zz,-} f'$ , the eMChA grows resonating way for  $\eta \lesssim 0.01$  due to the  $G_a^{zz,-}$ . Interestingly, this resonance mechanism is not important for  $M_{\text{orb}}$ ,  $\sigma_{yzz}$ , and the anomalous Hall conductivity  $\sigma_{xy}^{\text{AHE}}$ . Thus, the ‘‘QM-induced resonating enhancement’’ is specific for the eMChA.

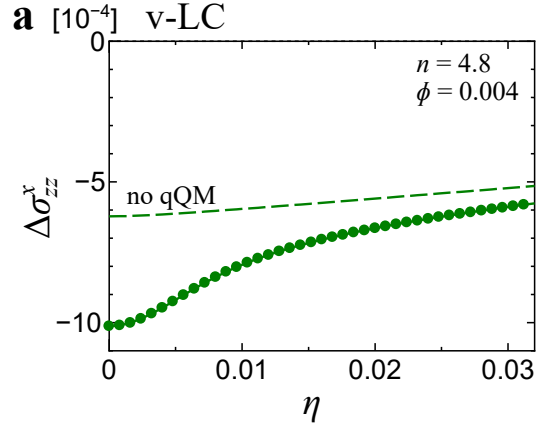


Fig. S4. **Enhancement of magnetoconductivity by QM.**  $\Delta\sigma_{zz}^x$  as a function of  $\eta$ . (Here,  $\gamma = 1$ .)  $\Delta\sigma_{zz}^x$  is enlarged for  $\eta \lesssim 0.01$  by the  $\eta$ -even QM. However,  $\Delta\sigma_{zz}^x$  is already large without the QM, so the QM-induced enhancement is only quantitative.

Finally, we briefly discuss the origin of the giant MR in kagome metal. For  $B_x < 1\text{T}$ , where  $\omega_H\tau < 1$ , the MR is proportional to  $B_x^2$ ;  $\rho_{zz}(B_x) = \rho_{zz}(0) + [-\Delta\sigma_{zz}^x/\sigma_{zz} - (\sigma_{zy}^{\text{norm},\alpha})^2/\sigma_{zz}\sigma_{yy}]B_x^2$ . The magnetoconductivity  $\Delta\sigma_{zz}^x$  is given in Eq. (S22). Here,  $\Delta\sigma_{zz}^x \propto \sum_{a,\mathbf{k}} f_a^{\{d^{x,z}\}} \gamma^{-3}$  and  $d^{x,z} = v^y v^{zz} - v^z v^{yz}$ . The  $((v^{zz})^2)^+$ -term in the integrand gives rise to the giant enhancement of the  $\rho_{zz}$  in the  $2 \times 2$  LC state, due to the QM term  $(g_a^{zz,+})^2 \sim G_a^{zz,+}(v_{ab}^{z,+} v_{ba}^{z,+})$ . Fig. S4 shows the obtained  $\Delta\sigma_{zz}^x$  of order  $O(B^2)$  as function of  $\eta$  ( $\gamma = 1$ ).  $\Delta\sigma_{zz}^x$  is enlarged for  $\eta \lesssim 0.01$  by the  $\eta$ -even QM. However,  $\Delta\sigma_{zz}^x$  is already large without the QM, so the QM-induced enhancement is only quantitative. In  $\text{CsV}_3\text{Sb}_5$ ,  $\rho_{zz}(B_x)$  does not saturate in the quantum limit  $\omega_H\tau \ll 1$  due to the open-orbit FS along the  $k_z$  axis [29]. Nearly



$B_x$ -linear MR for  $B_x \gg 1$  would originate from FSs with sharp corners in the  $2 \times 2$  LC phase [89].

**F: Numerical results of  $v_k^{zz,\pm}$ ,  $\tilde{v}_k^{zz,\pm}$ ,  $g_k^{zz,\pm}$ ,  $((g^{zz})^2)_k^\pm$  and  $G_k^{zz,\pm}$**

In this section, we perform the numerical study for  $X_k^\pm \equiv \sum_b X_{b,\mathbf{k}}^\pm (-f'(\epsilon_{b,\mathbf{k}}^0))$ , where  $X = v^{zz}$ ,  $\tilde{v}^{zz}$ ,  $g^{zz}$ ,  $(g^{zz})^2$ , and  $G^{zz}$ . Here,  $f(\epsilon)$  is Fermi distribution function. Note that  $f'(0) = -1/4T$ . Below, we set  $\eta = 0.024$  and  $T = 0.01$ .

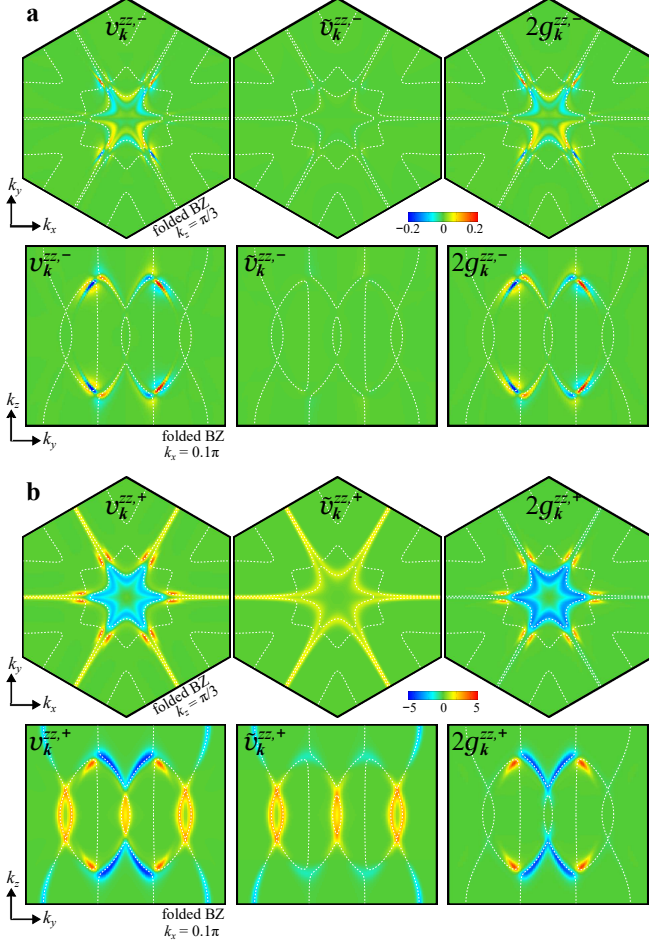


Fig. S5. Results of  $v_k^{zz,\pm}$ ,  $\tilde{v}_k^{zz,\pm}$ , and  $g_k^{zz,\pm}$ . **a.** Results of  $v_k^{zz,-}$ ,  $\tilde{v}_k^{zz,-}$ , and  $g_k^{zz,-}$  around the Fermi level, on the  $k_z = \pi/3$  plane and  $k_x = 0.1\pi$  plane. The broken lines represent the FSs. The relation  $v_k^{zz,-} \approx g_k^{zz,-}$  near the resonant positions is verified. **b.** Results of  $v_k^{zz,+}$ ,  $\tilde{v}_k^{zz,+}$ , and  $g_k^{zz,+}$ .

In Fig. S5 **a**, we show the  $\eta$ -odd functions  $v_k^{zz,-}$ ,  $\tilde{v}_k^{zz,-}$  and  $g_k^{zz,\pm}$ . We find that both  $v_k^{zz,-}$  and  $g_k^{zz,\pm}$  exhibit large values with sudden sign changes around the resonant position. Here, the relation  $v_k^{zz,-} \approx g_k^{zz,-}$  is obtained because  $\tilde{v}_k^{zz,-}$  is a small and smooth function of  $\mathbf{k}$ . The qQM term  $g_k^{zz,-}$  takes large values near the reso-

nant positions, where the pure-mix band reconstruction occurs, due to the mixture of the LC order ( $\eta$ ) in the pure-band and the large  $k_z$ -direction dispersion in the mix-band. As we have explained in the main text, the NLH conductivity is  $\sigma_{yzz} \propto \sum_{\mathbf{k}} g_k^{zz,-} v_k^{y,+} f'$ . Therefore, the NLH is strongly enlarged by the qQM, as we have explained in the main text.

We also show the  $\eta$ -even functions  $v_k^{zz,+}$ ,  $\tilde{v}_k^{zz,+}$  and  $g_k^{zz,+}$  in Fig. S5 **b**. Here,  $v_k^{zz,+}$  deviates from  $g_k^{zz,+}$  for wide area on the FSs because  $\tilde{v}_k^{zz,+}$  and  $g_k^{zz,+}$  are comparable in magnitude. Both  $v_k^{zz,+}$  and  $g_k^{zz,+}$  take large values mainly on the mix-band due to the large  $k_z$ -direction dispersion of the mix-band. (The pure-mix hybridization is not necessary for the enhancement of  $v_k^{zz,+}$  and  $g_k^{zz,+}$  because they are of order  $O(\eta^0)$ .)

In Fig. S6 **a**, we show  $\eta$ -odd functions  $((g^{zz})^2)_k^-$  and  $G_k^{zz,-}$  at  $\eta = 0.024$  and  $T = 0.01$ . These quantities exhibit drastic enhancement around the resonant positions. Both  $((g^{zz})^2)_k^-$  and  $G_k^{zz,-}$  are essentially positive for  $k_y < 0$  and negative for  $k_y > 0$ . (In contrast,  $g_k^{zz,-}$  exhibits the sudden sign change within the area  $k_y < 0$  (or  $k_y > 0$ ); see in Fig. S5 **a**.) Thus, the relation  $((g^{zz})^2)_k^- \propto G_k^{zz,-} \cdot (t_{m\perp})^2$  has been confirmed numerically. This relation is easily obtained in the two-band approximation. The QM term  $G_k^{zz,-}$  take large values near the resonant positions, where the pure-mix band reconstruction occurs, due to the coexistence between the LC order ( $\eta$ ) in the pure-band and the large  $k_z$ -direction dispersion in the mix-band. As we have explained in the main text, the eMChA conductivity is  $\sigma_{zzz,x} \propto \sum_{\mathbf{k}} ((g^{zz})^2)_k^- v_k^{y,+} f' \propto \sum_{\mathbf{k}} G_k^{zz,-} v_k^{y,+} f'$ , where  $v_k^{y,+} \propto k_y$ . Therefore, it is concluded that the giant eMChA originates from the odd- $\eta$  part of the QM.

We also show the  $\eta$ -even functions  $((g^{zz})^2)_k^+$  and  $G_k^{zz,+}$  in Fig. S6 **b**. Here,  $((g^{zz})^2)_k^+$  deviates from  $G_k^{zz,+}$  for wide area on the FSs. Both  $((g^{zz})^2)_k^+$  and  $G_k^{zz,+}$  take large values mainly on the mix-band due to the large  $k_z$ -direction dispersion of the mix-band. (Note that the pure-band with two-dimensional character is unimportant for  $((g^{zz})^2)_k^+$  and  $G_k^{zz,+}$  because they are of order  $O(\eta^0)$ .)

- 
- [1] E. Fradkin and S. A. Kivelson, *Ineluctable complexity*, Nat. Phys. **8**, 864 (2012).
  - [2] J. C. S. Davis and D.-H. Lee, *Concepts relating magnetic interactions, intertwined electronic orders, and strongly correlated superconductivity*, Proc. Natl. Acad. Sci. U.S.A. **110**, 17623 (2013).
  - [3] A. V. Chubukov, M. Khodas, and R. M. Fernandes, *Magnetism, Superconductivity, and Spontaneous Orbital Order in Iron-Based Superconductors: Which Comes First and Why?*, Phys. Rev. X **6**, 041045 (2016).
  - [4] R. M. Fernandes, P. P. Orth, and J. Schmalian, *Intertwined Vestigial Order in Quantum Materials: Nematic-*

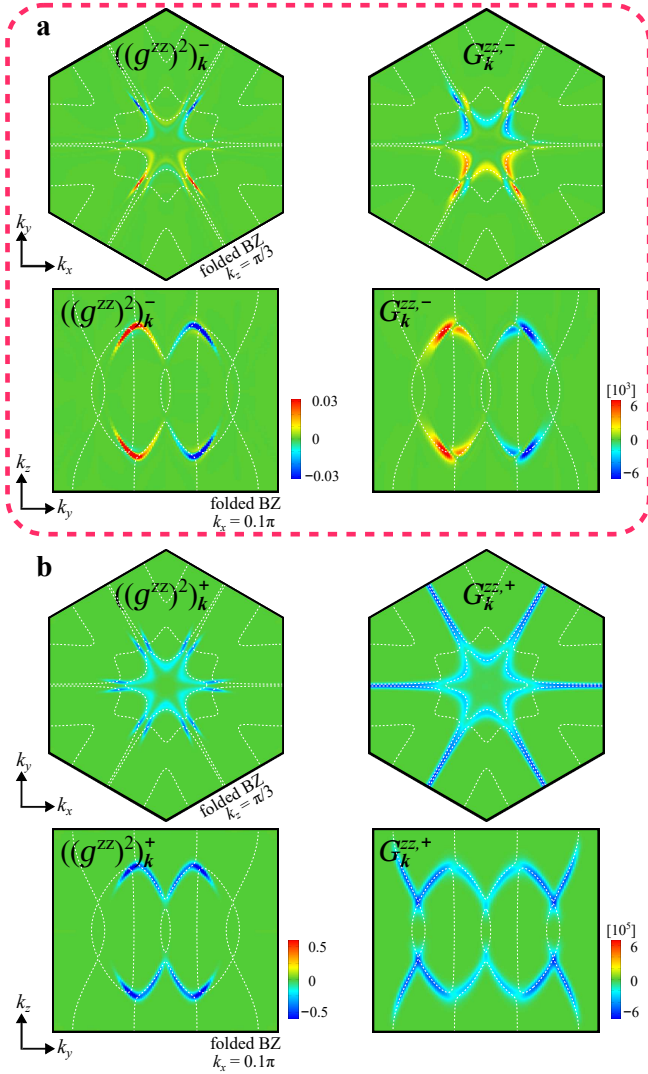


Fig. S6. Results of  $((g^{zz})^2)_k^\pm$  and  $G_k^{zz,\pm}$ . **a.** Results of  $((g^{zz})^2)_k^-$  and  $G_k^{zz,-}$  around the Fermi level, on the  $k_z = \pi/3$  plane and  $k_x = 0.1\pi$  plane. The broken lines represent the FSs. Here, the relation  $((g^{zz})^2)_k^- \propto G_k^{zz,-}$  near the resonant positions is verified numerically. This relation is significant for the QM-induced giant eMChA. **b.** Results of  $((g^{zz})^2)_k^+$  and  $G_k^{zz,+}$ .

ity and Beyond, *Annu. Rev. Condens. Matter Phys.* **10**, 133 (2019).

- [5] H. Kontani, R. Tazai, Y. Yamakawa, and S. Onari, *Unconventional density waves and superconductivities in Fe-based superconductors and other strongly correlated electron systems*, *Adv. Phys.* **70**, 355 (2021).
- [6] B. R. Ortiz, L. C. Gomes, J. R. Morey, M. Winiarski, M. Bordelon, J. S. Mangum, I. W. H. Oswald, J. A. Rodriguez-Rivera, J. R. Neilson, S. D. Wilson, E. Ertekin, T. M. McQueen, and E. S. Toberer, *New kagome prototype materials: discovery of  $KV_3Sb_5$ ,  $RbV_3Sb_5$ , and  $CsV_3Sb_5$* , *Phys. Rev. Materials* **3**, 094407 (2019).
- [7] B. R. Ortiz, S. M. L. Teicher, Y. Hu, J. L. Zuo, P. M. Sarte, E. C. Schueller, A. M. M. Abeykoon, M. J. Krogstad, S. Rosenkranz, R. Osborn, R. Seshadri, L. Balents, J. He, and S. D. Wilson,  *$CsV_3Sb_5$ : A  $\mathbb{Z}_2$  Topological Kagome Metal with a Superconducting Ground State*, *Phys. Rev. Lett.* **125**, 247002 (2020).

- [8] F. H. Yu, D. H. Ma, W. Z. Zhuo, S. Q. Liu, X. K. Wen, B. Lei, J. J. Ying, and X. H. Chen, *Unusual competition of superconductivity and charge-density-wave state in a compressed topological kagome metal*, *Nat. Commun.* **12**, 3645 (2021).
- [9] Y.-X. Jiang, J.-X. Yin, M. M. Denner, N. Shumiya, B. R. Ortiz, G. Xu, Z. Guguchia, J. He, M. S. Hossain, X. Liu, J. Ruff, L. Kautzsch, S. S. Zhang, G. Chang, I. Belopolski, Q. Zhang, T. A. Cochran, D. Multer, M. Litskevich, Z.-J. Cheng, X. P. Yang, Z. Wang, R. Thomale, T. Neupert, S. D. Wilson, and M. Z. Hasan, *Unconventional chiral charge order in kagome superconductor  $KV_3Sb_5$* , *Nat. Mater.* **20**, 1353 (2021).
- [10] H. Li, H. Zhao, B. R. Ortiz, T. Park, M. Ye, L. Balents, Z. Wang, S. D. Wilson, and I. Zeljkovic, *Rotation symmetry breaking in the normal state of a kagome superconductor  $KV_3Sb_5$* , *Nat. Phys.* **18**, 265 (2022).
- [11] M. Roppongi, K. Ishihara, Y. Tanaka, K. Ogawa, K. Okada, S. Liu, K. Mukasa, Y. Mizukami, Y. Uwatoko, R. Grasset, M. Konczykowski, B. R. Ortiz, S. D. Wilson, K. Hashimoto, and T. Shibauchi, *Bulk evidence of anisotropic s-wave pairing with no sign change in the kagome superconductor  $CsV_3Sb_5$* , *Nat. Commun.* **14**, 667 (2023).
- [12] W. Zhang, X. Liu, L. Wang, C. Wai T., Z. Wang, S. T. Lam, W. Wang, J. Xie, X. Zhou, Y. Zhao, S. Wang, J. Tallon, K. T. Lai, and S. K. Goh, *Nodeless superconductivity in kagome metal  $CsV_3Sb_5$  with and without time reversal symmetry breaking*, *Nano Lett.*, **23**, 872 (2023).
- [13] M. L. Kiesel, C. Platt, and R. Thomale, *Unconventional Fermi Surface Instabilities in the Kagome Hubbard Model*, *Phys. Rev. Lett.* **110**, 126405 (2013).
- [14] W.-S. Wang, Z.-Z. Li, Y.-Y. Xiang, and Q.-H. Wang, *Competing electronic orders on kagome lattices at van Hove filling*, *Phys. Rev. B* **87**, 115135 (2013).
- [15] X. Wu, T. Schwemmer, T. Müller, A. Consiglio, G. Sangiovanni, D. Di Sante, Y. Iqbal, W. Hanke, A. P. Schnyder, M. M. Denner, M. H. Fischer, T. Neupert, and R. Thomale, *Nature of Unconventional Pairing in the Kagome Superconductors  $AV_3Sb_5$  ( $A = K, Rb, Cs$ )*, *Phys. Rev. Lett.* **127**, 177001 (2021).
- [16] M. M. Denner, R. Thomale, and T. Neupert, *Analysis of Charge Order in the Kagome Metal  $AV_3Sb_5$  ( $A = K, Rb, Cs$ )*, *Phys. Rev. Lett.* **127**, 217601 (2021).
- [17] T. Park, M. Ye, and L. Balents, *Electronic instabilities of kagome metals: Saddle points and Landau theory*, *Phys. Rev. B* **104**, 035142 (2021).
- [18] Y.-P. Lin and R. M. Nandkishore, *Complex charge density waves at Van Hove singularity on hexagonal lattices: Haldane-model phase diagram and potential realization in the kagome metals  $AV_3Sb_5$  ( $A = K, Rb, Cs$ )*, *Phys. Rev. B* **104**, 045122 (2021).
- [19] R. Tazai, Y. Yamakawa, S. Onari, and H. Kontani, *Mechanism of exotic density-wave and beyond-Migdal unconventional superconductivity in kagome metal  $AV_3Sb_5$  ( $A = K, Rb, Cs$ )*, *Sci. Adv.* **8**, eabl4108 (2022).
- [20] R. Tazai, Y. Yamakawa, and H. Kontani, *Charge-loop current order and  $Z_3$  nematicity mediated by bond order fluctuations in kagome metals*, *Nat. Commun.* **14**, 7845 (2023).
- [21] Z. Guguchia, C. Mielke III, D. Das, R. Gupta, J.-

- X. Yin, H. Liu, Q. Yin, M.H. Christensen, Z. Tu, C. Gong, N. Shumiya, Ts. Gamsakhurdashvili, M. Elender, Pengcheng Dai, A. Amato, Y. Shi, H.C. Lei, R.M. Fernandes, M.Z. Hasan, H. Luetkens, and R. Khasanov, *Tunable nodal kagome superconductivity in charge ordered  $RbV_3Sb_5$* , Nat. Commun. **14**, 153 (2023).
- [22] L. Yu, C. Wang, Y. Zhang, M. Sander, S. Ni, Z. Lu, S. Ma, Z. Wang, Z. Zhao, H. Chen, K. Jiang, Y. Zhang, H. Yang, F. Zhou, X. Dong, S. L. Johnson, M. J. Graf, J. Hu, H.-J. Gao, and Z. Zhao, *Evidence of a hidden flux phase in the topological kagome metal  $CsV_3Sb_5$* , arXiv:2107.10714 (available at <https://arxiv.org/abs/2107.10714>).
- [23] C. Mielke, D. Das, J.-X. Yin, H. Liu, R. Gupta, Y.-X. Jiang, M. Medarde, X. Wu, H. C. Lei, J. Chang, P. Dai, Q. Si, H. Miao, R. Thomale, T. Neupert, Y. Shi, R. Khasanov, M. Z. Hasan, H. Luetkens, and Z. Guguchia, *Time-reversal symmetry-breaking charge order in a kagome superconductor*, Nature **602**, 245 (2022).
- [24] R. Khasanov, D. Das, R. Gupta, C. Mielke, M. Elender, Q. Yin, Z. Tu, C. Gong, H. Lei, E. T. Ritz, R. M. Fernandes, T. Birol, Z. Guguchia, and H. Luetkens, *Time-reversal symmetry broken by charge order in  $CsV_3Sb_5$* , Phys. Rev. Research **4**, 023244 (2022).
- [25] R. Tazai, Y. Yamakawa and H. Kontani, *Drastic magnetic-field-induced chiral current order and emergent current-bond-field interplay in kagome metals*, Proc. Natl. Acad. of Sci. **121**, e2303476121 (2024).
- [26] C. Guo, G. Wagner, C. Putzke, D. Chen, K. Wang, L. Zhang, M. G. Amigo, I. Errea, M. G. Vergniory, C. Felser, M. H. Fischer, T. Neupert, and P. J. W. Moll, *Correlated order at the tipping point in the kagome metal  $CsV_3Sb_5$* , Nature Physics **20**, 579 (2024).
- [27] S.-Y. Yang, Y. Wang, B. R. Ortiz, D. Liu, J. Gayles, E. Derunova, R. Gonzalez-Hernandez, L. Šmejkal, Y. Chen, S. S. P. Parkin, S. D. Wilson, E. S. Toberer, T. McQueen, and M. N. Ali, *Giant, unconventional anomalous Hall effect in the metallic frustrated magnet candidate,  $KV_3Sb_5$* , Sci. Adv. **6**, eabb6003 (2020).
- [28] F. H. Yu, T. Wu, Z. Y. Wang, B. Lei, W. Z. Zhuo, J. J. Ying, and X. H. Chen, *Concurrence of anomalous Hall effect and charge density wave in a superconducting topological kagome metal*, Phys. Rev. B **104**, L041103 (2021).
- [29] C. Guo, C. Putzke, S. Konyzheva, X. Huang, M. Gutierrez-Amigo, I. Errea, D. Chen, M. G. Vergniory, C. Felser, M. H. Fischer, T. Neupert, and P. J. W. Moll, *Switchable chiral transport in charge-ordered Kagome metal  $CsV_3Sb_5$* , Nature **611**, 461 (2022).
- [30] Y. Xu, Z. Ni, Y. Liu, B. R. Ortiz, S. D. Wilson, B. Yan, L. Balents, and L. Wu, *Universal three-state nematicity and magneto-optical Kerr effect in the charge density waves in  $AV_3Sb_5$  ( $A=Cs, Rb, K$ )*, Nat. Phys. **18**, 1470 (2022).
- [31] T. Asaba, A. Onishi, Y. Kageyama, T. Kiyosue, K. Ohtsuka, S. Suetsugu, Y. Kohsaka, T. Gaggli, Y. Kasahara, H. Murayama, K. Hashimoto, R. Tazai, H. Kontani, B. R. Ortiz, S. D. Wilson, Q. Li, H.-H. Wen, T. Shibauchi, and Y. Matsuda, *Evidence for an odd-parity nematic phase above the charge density wave transition in kagome metal  $CsV_3Sb_5$* , arXiv:2309.16985 (available at <https://arxiv.org/abs/2309.16985>). (to be published in Nat. Phys.)
- [32] S. Zhou and Z. Wang, *Chern Fermi pocket, topological pair density wave, and charge- $4e$  and charge- $6e$  superconductivity in kagome superconductors*, Nat. Commun. **13**, 7288 (2022).
- [33] Y.-M. Wu, R. Thomale, S. Raghu, *Sublattice Interference promotes Pair Density Wave order in Kagome Metals*, Phys. Rev. B **108**, L081117 (2023).
- [34] Z. Pan, C. Lu, F. Yang, C. Wu, *Frustrated superconductivity and charge- $6e$  ordering*, arXiv:2209.13745 (available at <https://arxiv.org/abs/2209.13745>).
- [35] Y. Tokura and N. Nagaosa, *Nonreciprocal responses from non-centrosymmetric quantum materials*, Nature communications, **9**, 3740 (2018).
- [36] J. Orenstein, J. E. Moore, T. Morimoto, D. H. Torchinsky, J. W. Harter, and D. Hsieh, *Topology and symmetry of quantum materials via nonlinear optical responses*, Annual Review of Condensed Matter Physics **12**, 247 (2021).
- [37] Q. Ma, K. Krishna, X. Roshan, K. Su-Yang, H. L. Frank, and J. C. W. Song, *Photocurrent as a multiphysics diagnostic of quantum materials*, Nature Reviews Physics, **5**, 170 (2023).
- [38] G. L. J. A. Rikken and E. Raupach, *Observation of magneto-chiral dichroism*, Nature, **390**, 493 (1997).
- [39] G. L. J. A. Rikken, J. Fölling, P. and Wyder, *Electrical Magnetochiral Anisotropy*, Phys. Rev. Lett., **87**, 236602 (2001).
- [40] R. Wakatsuki, Y. Saito, S. Hoshino, Y. M. Itahashi, T. Ideue, M. Ezawa, Y. Iwasa, and N. Nagaosa, *Nonreciprocal charge transport in noncentrosymmetric superconductors*, Science advances **3**, e1602390 (2017).
- [41] T. Yokouchi, Y. Ikeda, T. Morimoto, and Y. Shiomi, *Giant magnetochiral anisotropy in Weyl semimetal  $WTe_2$  induced by diverging Berry curvature*, Phys. Rev. Lett., **130**, 136301 (2023).
- [42] R. Aoki, Y. Kousaka, and Y. Togawa, *Anomalous non-reciprocal electrical transport on chiral magnetic order*, Phys. Rev. Lett. **122**, 057206 (2019).
- [43] T. Yokouchi, *et al.*, *Electrical magnetochiral effect induced by chiral spin fluctuations*, Nat. Commun. **8**, 866 (2017).
- [44] H. Zhao *et al.*, *Cascade of correlated electron states in the kagome superconductor  $CsV_3Sb_5$* , Nature **599**, 216 (2021).
- [45] H. Li, H. Zhao, B. R. Ortiz, Y. Oey, Z. Wang, S. D. Wilson, and I. Zeljkovic, *Unidirectional coherent quasiparticles in the high-temperature rotational symmetry broken phase of  $AV_3Sb_5$  kagome superconductors*, Nat. Phys. **19**, 637 (2023).
- [46] C. Guo, M. R. van Delft, M. Gutierrez-Amigo, D. Chen, C. Putzke, G. Wagner, M. H. Fischer, T. Neupert, I. Errea, M. G. Vergniory, S. Wiedmann, C. Felser, and P.J. W. Moll, *Distinct switching of chiral transport in the kagome metals  $KV_3Sb_5$  and  $CsV_3Sb_5$* , npj Quantum Materials, **9**, 20 (2024).
- [47] R. Resta, *Macroscopic polarization in crystalline dielectrics: the geometric phase approach* Rev. Mod. Phys. **66**, 899 (1994).
- [48] N. Marzari and D. Vanderbilt, *Maximally localized generalized Wannier functions for composite energy bands*, Phys. Rev. B **56**, 12847 (1997).
- [49] R. Resta, *The insulating state of matter: a geometrical theory*, The European Physical Journal B, **79**, 121 (2011).
- [50] C.-K. Chiu, J. C. Y. Teo, A. P. Schnyder, and S. Ryu, *Classification of topological quantum matter with symmetries* Rev. Mod. Phys. **88**, 035005 (2016).
- [51] Q. Ma, *et al.* *Photocurrent as a multiphysics diagnosis*

- tic of quantum materials* Nature Reviews Physics **5**, 170 (2023).
- [52] N. Nagaosa, J. Sinova, S. Onoda, A. H. MacDonald, and N. P. Ong, *Anomalous hall effect*, Rev. Mod. Phys. **82**, 1539 (2010).
- [53] H. Kontani, *Anomalous transport phenomena in Fermi liquids with strong magnetic fluctuations*, Rep. Prog. Phys. **71**, 026501 (2008).
- [54] H. Kontani, T. Tanaka, D. S. Hirashima, K. Yamada, and J. Inoue, *Giant Orbital Hall Effect in Transition Metals: Origin of Large Spin and Anomalous Hall Effects*, Phys. Rev. Lett. **102**, 016601 (2009).
- [55] H. Kontani, T. Tanaka, and K. Yamada, *Intrinsic anomalous Hall effect in ferromagnetic metals studied by the multi-d-orbital tight-binding model*, Phys. Rev. B **75**, 184416 (2007).
- [56] I. Sodemann and L. Fu, *Quantum nonlinear Hall effect induced by Berry curvature dipole in time-reversal invariant materials*, Phys. Rev. Lett. **115**, 216806 (2015).
- [57] P. Törmä, S. Peotta, and B. A. Bernevig, *Superconductivity, superfluidity and quantum geometry in twisted multilayer systems*, Nature Reviews Physics **4**, 528 (2022).
- [58] A. Gao, Y.-F. Liu, J.-X. Qiu, B. Ghosh, T. V. Trevisan, Y. Onishi, C. Hu, T. Qian, H.-J. Tien, S.-W. Chen, M. Huang, D. Berube, H. Li, C. Tzschaschel, T. Dinh, Z. Sun, S.-C. Ho, S.-W. Lien, B. Singh, K. Watanabe, T. Taniguchi, D. C. Bell, H. Lin, T.-R. Chang, C. R. Du, A. Bansil, L. Fu, N. Ni, P. P. Orth, Q. Ma, and S.-Y. Xu, *Quantum metric nonlinear Hall effect in a topological antiferromagnetic heterostructure*, Science **381**, 181 (2023).
- [59] X. Feng, K. Jiang, Z. Wang, and J. Hu, *Chiral flux phase in the Kagome superconductor  $AV_3Sb_5$* , Sci. Bull. **66**, 1384 (2021).
- [60] C. M. Varma, *Non-Fermi-liquid states and pairing instability of a general model of copper oxide metals*, Phys. Rev. B **55**, 14554 (1997).
- [61] C. Weber, T. Giamarchi, and C. M. Varma, *Phase Diagram of a Three-Orbital Model for High- $T_c$  Cuprate Superconductors*, Phys. Rev. Lett. **112**, 117001 (2014).
- [62] A. A. Nersisyan, G. I. Japaridze, and I. G. Kimeridze, *Low-temperature magnetic properties of a two-dimensional spin nematic state*, J. Phys.: Condens. Matter **3**, 3353 (1991).
- [63] S. Onari and H. Kontani, *Self-consistent Vertex Correction Analysis for Iron-based Superconductors: Mechanism of Coulomb Interaction-Driven Orbital Fluctuations*, Phys. Rev. Lett. **109**, 137001 (2012).
- [64] M. Tsuchiizu, Y. Ohno, S. Onari, and H. Kontani, *Orbital Nematic Instability in the Two-Orbital Hubbard Model: Renormalization-Group + Constrained RPA Analysis*, Phys. Rev. Lett. **111**, 057003 (2013).
- [65] M. Tsuchiizu, K. Kawaguchi, Y. Yamakawa, and H. Kontani, *Multistage electronic nematic transitions in cuprate superconductors: A functional-renormalization-group analysis*, Phys. Rev. B **97**, 165131 (2018).
- [66] Y. Yamakawa and H. Kontani, *Spin-Fluctuation-Driven Nematic Charge-Density Wave in Cuprate Superconductors: Impact of Aslamazov-Larkin Vertex Corrections*, Phys. Rev. Lett. **114**, 257001 (2015).
- [67] Y. Yamakawa, S. Onari, and H. Kontani, *Nematicity and Magnetism in FeSe and Other Families of Fe-Based Superconductors*, Phys. Rev. X **6**, 021032 (2016).
- [68] S. Onari, Y. Yamakawa, and H. Kontani, *Sign-Reversing Orbital Polarization in the Nematic Phase of FeSe due to the  $C_2$  Symmetry Breaking in the Self-Energy*, Phys. Rev. Lett. **116**, 227001 (2016).
- [69] R. Tazai, S. Matsubara, Y. Yamakawa, S. Onari, and H. Kontani, *A Rigorous Formalism of Unconventional Symmetry Breaking in Fermi Liquid Theory and Its Application to Nematicity in FeSe*, Phys. Rev. B **107**, 035137 (2023).
- [70] R. Tazai, Y. Yamakawa, and H. Kontani, *Emergence of charge loop current in the geometrically frustrated Hubbard model: A functional renormalization group study*, Phys. Rev. B **103**, L161112 (2021).
- [71] R. Tazai, Y. Yamakawa, M. Tsuchiizu, and H. Kontani, *d- and p-wave Quantum Liquid Crystal Orders in Cuprate Superconductors,  $\kappa$ -(BEDT-TTF) $_2X$ , and Coupled Chain Hubbard Models: Functional-renormalization-group Analysis*, J. Phys. Soc. Jpn. **90**, 111012 (2021).
- [72] S. Onari and H. Kontani,  *$SU(4)$  Valley+Spin Fluctuation Interference Mechanism for Nematic Order in Magic-Angle Twisted Bilayer Graphene: The Impact of Vertex Corrections*, Phys. Rev. Lett. **128**, 066401 (2022).
- [73] R. Nandkishore, L. S. Levitov, A. V. Chubukov, *Chiral superconductivity from repulsive interactions in doped graphene*, Nat. Phys. **8**, 158 (2012).
- [74] J.-Wei D., Z. Wang, S. Zhou, *Loop-current charge density wave driven by long-range Coulomb repulsion on the kagome lattice*, Phys. Rev. B **107**, 045127 (2023).
- [75] H. D. Scammell, J. Ingham, T. Li, and O. P. Sushkov, *Chiral excitonic order from twofold van Hove singularities in kagome metals*, Nat. Commun. **14**, 605 (2023).
- [76] Y. Hu, X. Wu, B. R. Ortiz, S. Ju, X. Han, J. Ma, N. C. Plumb, M. Radovic, R. Thomale, S. D. Wilson, A. P. Schnyder, and M. Shi, *Rich nature of Van Hove singularities in Kagome superconductor  $CsV_3Sb_5$* , Nature **13**, 2220 (2022).
- [77] Y. Luo, S. Peng, S. M. L. Teicher, L. Huai, Y. Hu, B. R. Ortiz, Z. Wei, J. Shen, Z. Ou, B. Wang, Y. Miao, M. Guo, M. Shi, S. D. Wilson, and J.-F. He, *Distinct band reconstructions in kagome superconductor  $CsV_3Sb_5$* , Phys. Rev. B **105**, L241111 (2022).
- [78] D. Bohm, Phys. Rev. **75**, 502 (1949).
- [79] Y. Xing, S. Bae, E. Ritz, F. Yang, T. Birol, A. N. C. Salinas, B. R. Ortiz, S. D. Wilson, Z. Wang, R. M. Fernandes, and V. Madhavan, *Optical Manipulation of the Charge Density Wave state in  $RbV_3Sb_5$* , arXiv:2308.04128 (available at <https://arxiv.org/abs/2308.04128>).
- [80] H. W. S. Arachchige, W. R. Meier, M. Marshall, T. Matsumoto, R. Xue, M. A. McGuire, R. P. Hermann, H. Cao, and D. Mandrus, *Charge Density Wave in Kagome Lattice Intermetallic  $ScV_6Sn_6$* , Phys. Rev. Lett. **129**, 216402 (2022).
- [81] H. Hu, Y. Jiang, D. Calug, X. Feng, D. Subires, M. G. Vergniory, C. Felser, S. Blanco-Canosa, and B. A. Bernevig, *Kagome Materials I: SG 191,  $ScV_6Sn_6$ . Flat Phonon Soft Modes and Unconventional CDW Formation: Microscopic and Effective Theory*, arXiv:2305.15469 (available at <https://arxiv.org/abs/2305.15469>).
- [82] A. Korshunov, H. Hu, D. Subires, Y. Jiang, D. Calugaru, X. Feng, A. Rajapitamahuni, C. Yi, S. Roychowdhury, M. G. Vergniory, J. Stempfer, C. Shekhar, E. Vescovo, D. Chernyshov, A. H. Said, A. Bosak, C. Felser, B. Andrei Bernevig, S. Blanco-Canosa, *Softening of a flat phonon mode in the kagome  $ScV_6Sn_6$* , arXiv:2304.09173 (avail-

- able at <https://arxiv.org/abs/2304.09173>).
- [83] Z. Guguchia, D.J. Gawryluk, Soohyeon Shin, Z. Hao, C. Mielke III, D. Das, I. Plokhikh, L. Liborio, K. Shenton, Y. Hu, V. Sazgari, M. Medarde, H. Deng, Y. Cai, C. Chen, Y. Jiang, A. Amato, M. Shi, M.Z. Hasan, J.-X. Yin, R. Khasanov, E. Pomjakushina, and H. Luetkens, *Hidden magnetism uncovered in charge ordered bilayer kagome material  $ScV_6Sn_6$* , arXiv:2304.06436 (available at <https://arxiv.org/abs/2304.06436>).
- [84] D. Ceresoli, T. Thonhauser, D. Vanderbilt, and R. Resta, *Orbital magnetization in crystalline solids: Multi-band insulators, Chern insulators, and metals*, Phys. Rev. B **74**, 024408 (2006).
- [85] J. Shi, G. Vignale, D. Xiao, and Q. Niu, *Quantum theory of orbital magnetization and its generalization to interacting systems*, Phys. Rev. Lett. **99**, 197202 (2007).
- [86] T. Tanaka, H. Kontani, M. Naito, T. Naito, D. S. Hirschman, K. Yamada, and J. Inoue, *Intrinsic spin Hall effect and orbital Hall effect in 4d and 5d transition metals*, Phys. Rev. B **77**, 165117 (2008).
- [87] D. Xiao, M.-C. Chang, and Q. Niu, *Berry phase effects on electronic properties*, Rev. Mod. Phys. **82**, 1959 (2010).
- [88] X. Liu, I. Souza, and S. S. Tsirkin, *Electrical magnetochiral anisotropy in trigonal tellurium from first principles*, arXiv:2303.10164.
- [89] A. A. Abrikosov, *Quantum linear magnetoresistance*, Europhys. Lett. **49**, 789 (2000).